Chemical Science

ROYAL SOCIETY OF CHEMISTRY

REVIEW

View Article Online
View Journal | View Issue



Cite this: *Chem. Sci.*, 2025, **16**, 2136

# Opportunities and challenges of lead-free metal halide perovskites for luminescence

Run Tan,[b] Zhenyu Liu,[c] Zhigang Zang *[ab] and Shuangyi Zhao*[b]

Received 22nd June 2024
Accepted 23rd October 2024

DOI: 10.1039/d4sc04119d

rsc.li/chemical-science

Metal halide perovskites (MHPs) have been developed rapidly for application in light-emitting diodes (LEDs), lasers, solar cells, photodetectors and other fields in recent years due to their excellent photoelectronic properties, and they have attracted the attention of many researchers. Perovskite LEDs (PeLEDs) show great promise for next-generation lighting and display technologies, and the external quantum efficiency (EQE) values of polycrystalline thin-film PeLEDs exceed 20%, which is undoubtedly a big breakthrough in lighting and display fields. However, the toxicity and instabilities of lead-based MHPs remain major obstacles limiting their further commercial applications. The exploration and development of lead-free MHPs (LFMHPs) are regarded as the most facile strategies to solve these problems. Compared with lead-based perovskites, LFMHPs exhibit better stabilities and broadband emission. With continuous development of LFMHPs, their photoluminescence quantum yields (PLQYs) have reached 99%, facilitating their use as ideal emitters. In this review, the structures and features of LFMHPs are analyzed, and the preparation methods of LFMHPs with various structures and configurations are discussed. Then, the mechanisms and strategies for improving the emission performance of white LEDs based on LFMHPs are demonstrated. Finally, their challenges in commercial production and perspectives are prospected.



## Introduction

In the field of solid-state lighting technology, white-light-emitting diodes (WLEDs) have been identified as ideal light sources to replace incandescent bulbs due to their long lifetime, low energy consumption, wide spectrum, and controllability of color temperature.[1] Light-emitting diodes (LEDs) were first demonstrated from the development of gallium nitride (GaN)-based semiconductors in the early 1990s.[2] As one of the 2014 Nobel Prize winners, Nakamura created a representative high-brightness blue GaN-LED with an external quantum efficiency of 7.20% in 1993, which shows good prospects for application in WLEDs. Therefore, WLEDs have gradually been recognized as excellent candidates in cost-effective and high-efficiency solid-state lighting.[1–10]

As a new type of semiconductor material, metal halide perovskites (MHPs) possess many advantages,[11] such as high photoluminescence quantum yields, tunable bandgaps,[12] high carrier mobility,[13] solution processibility,[14] and low preparation cost.[15] All of these superior photoelectronic properties give MHPs great potential to perform well in LEDs.[11,13,14,16–23] MHPs are materials with the formula $ABX_3$ with a crystal structure similar to that of the mineral perovskite $CaTiO_3$, where A is a monovalent cation, such as $CH_3NH_3^+$ ($MA^+$), $CH(NH_2)^+$ ($FA^+$), and $Cs^+$; B is a bivalent metal cation, such as $Pb^{2+}$, $Sn^{2+}$, $Cu^{2+}$, ($Ag^+$ and $Bi^{3+}$ are double perovskites); and X represents the halide anions, including $Cl^-$, $Br^-$, and $I^-$. By changing the halogen and cation composition,[24] the structures and chemical bonds of MHPs can be regulated, resulting in changes to their photoelectronic properties. With the further study of perovskites, novel $A_2BX_4$, $A_3BX_6$ and $A_3B_2X_5$ metal halide perovskites are now being researched in addition to the classic $ABX_3$ metal halides. Since Tan *et al.* fabricated the first LEDs based on solution-processed organometallic halide perovskites in 2014,[25] perovskite-based LEDs have been developed. In just a few years, internal quantum efficiencies (IQEs) and external quantum efficiencies (EQEs) of perovskite LEDs (PeLEDs) increased from 3.4% and 0.76% in the near-infrared region and 0.4% and 0.1% in the green-light region to more than 20% in the near-infrared[26,27] and green-light[28] regions, respectively. Due to the excellent photoelectronic performance of MHPs and the rapid development of PeLEDs, certain progress has been made in the material preparation and device fabrication of WLEDs. For example, warm and cold WLEDs were achieved by incorporating 1% and 10% $Sb^{3+}$ doped $Cs_2ZrCl_6$ on a 310 nm UV-LED chip, respectively.[29] However, the inherent toxicity of lead, the complex preparation process, and the low operational lifetime of PeLEDs, as well as their instability under high temperature, light, humidity and other conditions,[16,17,30] limits the application of MHPs in solid-state lighting.[31,32]

[a]*School of Information Science and Engineering, Yanshan University, Qinhuangdao 066004, P. R. China. E-mail: zangzg@cqu.edu.cn*

[b]*Key Laboratory of Optoelectronic Technology and Systems (Ministry of Education), Chongqing University, Chongqing 400044, China. E-mail: shyzhao@cqu.edu.cn*

[c]*CDGM Glass Company Limited, Chengdu, Sichuan, China*

To solve these problems, lead-free metal halide perovskites (LFMHPs), in which $Pb^{2+}$ ions are completely replaced by bivalent cations, such as $Sn^{2+}$, $Ge^{2+}$, and $Zn^{2+}$,[33] have been studied and applied in photoelectronic applications. Additionally, ions with different valence states can also replace $Pb^{2+}$ ions, such as trivalent $Sb^{3+}$,[34] $Eu^{3+}$, $Tb^{3+}$,[35] and monovalent $Cu^{+}$,[36] and this occurs *via* heterovalent substitution. At the same time, replacing $Pb^{2+}$ in a perovskite with monovalent, trivalent and quadrivalent cations, as well as vacancies, can not only improve perovskite stability, but also lead to enhancement of their photoelectronic properties. For LFMHPs, their band gap values can be adjusted according to the different metal components, so that more stable electroluminescence in LEDs can be obtained. The outstanding performance of LFMHPs has attracted the attention of many researchers, and up to now, there has been a lot of progress in WLEDs based on LFMHPs. $Sb^{3+}$-doped $Cs_2InCl_5 \cdot H_2O$:$Sb^{3+}$ exhibits broadband yellow light emission, and its PLQY is as high as 95.5%.[34] $Cs_2AgInCl_6$ prepared by Li *et al.* exhibited an enhanced PLQY of 87.2%, assisted by sodium ($Na^{+}$) alloying and bismuth ($Bi^{3+}$) doping, and was used in WLEDs to achieve efficient white-light emission with International Commission on Illumination (CIE) color coordinates of (0.38, 0.44)[37] and a color render index (CRI) of 87.8, showing remarkable operational stability under ambient conditions. In this review, the structures and characteristics of LFMHPs are firstly analysed, and preparation methods of LFMHPs with different structures and configurations are discussed. Furthermore, mechanisms, key parameters and strategies for improving the luminous efficiencies of WLEDs based on LFMHPs are described. Finally, their challenges and prospects in commercial applications are discussed (Fig. 1).

## Structures, dimension and optical properties of LFMHPs

As is well-known, perovskite configurations can be divided into zero-dimensional (0D), one-dimensional (1D), two-dimensional (2D) and three-dimensional (3D) according to their atomic arrangement order. In addition, perovskites can exist in various structures, such as nanocrystals (NCs), powders, thin films, and single crystals. Different structures can affect the photoelectronic performance of LFMHPs and PeLEDs.[38] Similar to traditional 3D Pb-based perovskites, 3D LFMHPs possess a 3D configuration, where corner-shared $[BX_6]^{4-}$ octahedra are the basic units.[39] In a $[BX_6]^{4-}$ octahedron, a metal cation is located in the center of the octahedron surrounded by monovalent cations (*e.g.* $Cs^{+}$, $Rb^{+}$, and $CH_3NH_3^{+}$). For example, Sn(II)-based $ASnX_3$ perovskites (X = $Cl^{-}$, $Br^{-}$, $I^{-}$) show a similar three-dimensional configuration, as shown in Fig. 2a.[40] By introducing larger cations such as butylammonium (BA) and phenethylamine (PEA), the 3D octahedral framework can be isolated into octahedral layers with shared angles, resulting in reduction of dimension from 3D to 2D. 2D perovskites can be viewed as a plate or layer cut along a crystallographic direction. By cutting 3D perovskites along the (001) plane, Ruddlesden–Popper-type ($R_2A_{n-1}M_nX_{3n+1}$, R = $1^{+}$ cation) or Dion–Jacobson-type ($RA_{n-1}M_nX_{3n+1}$, R = $2^{+}$ cation) perovskites can be obtained.[46,47] For two typical perovskites with layered structures, A-site ions are regarded as organic ligands. The dimension of LFMHPs can be further reduced to 1D with side- and angular-shared chains (formula $A_3BX_6$),[48] and unconnected (isolated) octahedral 0D structures (formula $A_3B_2X_6$).[49]

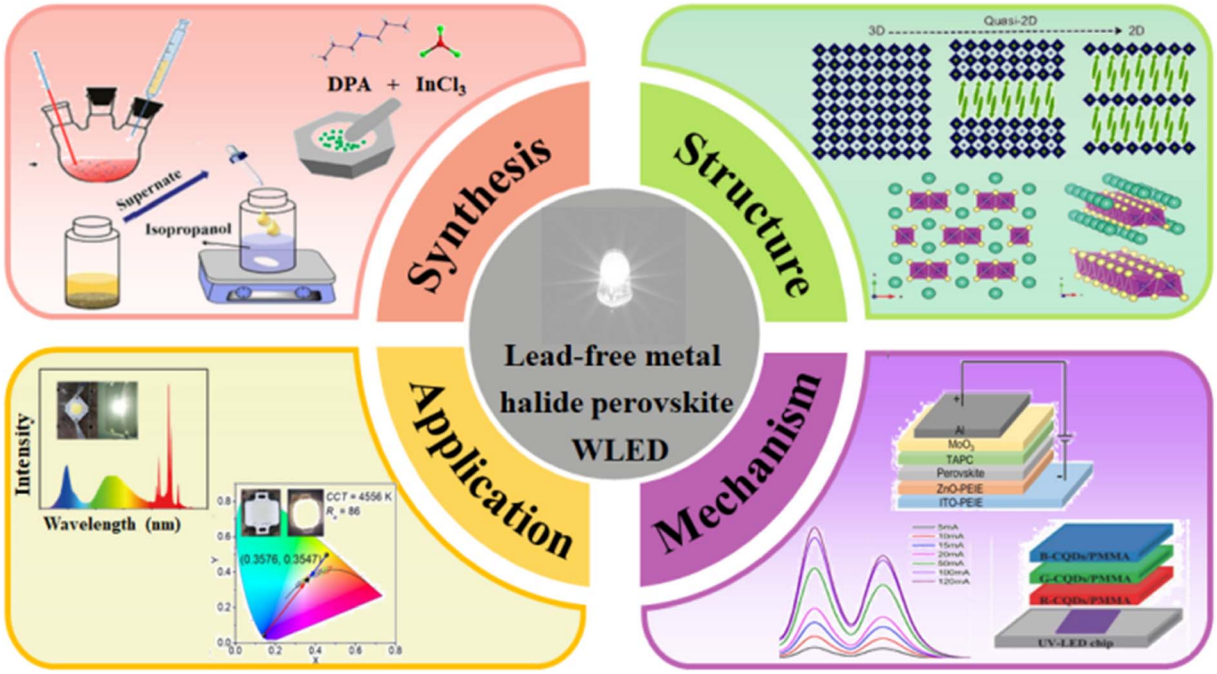


Fig. 1 Summary of the review, which includes synthesis and structures of LFMHPs, as well as mechanisms and applications of WLEDs based on LFMHPs.

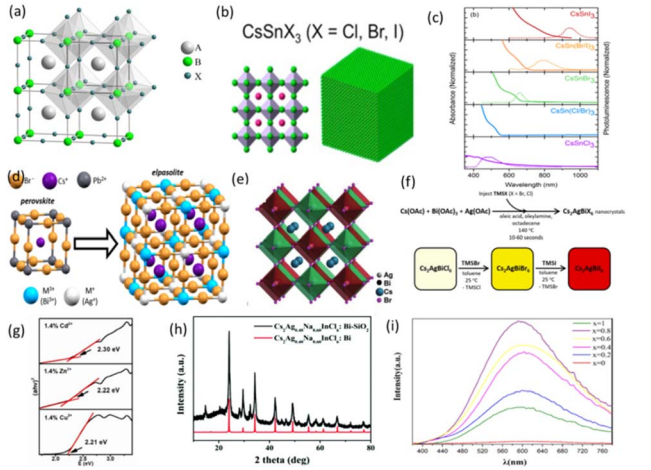


Fig. 2 (a) $ABX_3$ perovskite structure. $BX_6$ corner-sharing octahedra are in evidence.[40] Copyright 2008 American Chemical Society. (b) Structure of $CsSnX_3$.[41] Copyright 2016 American Chemical Society. (c) Absorption and steady-state PL of NCs containing pure and mixed halogens.[41] Copyright 2016 American Chemical Society. (d) Structure of double perovskites with $M^+$ and $M^{3+}$ ions replacing $Pb^{2+}$ ions.[42] Copyright 2018 American Chemical Society. (e) Crystal structure of cubic $Cs_2AgBiBr_6$.[43] Copyright 2018 American Chemical Society. (f) Synthesis diagram of $Cs_2AgBiX_6$ NCs.[42] Copyright 2018 American Chemical Society. (g) Tauc plots for 1.4% $Cd^{2+}$, 1.4% $Zn^{2+}$, and 1.4% $Cu^{2+}$-doped $Cs_2AgInCl_6$, respectively.[44] Copyright 2020 American Chemical Society. (h) XRD of $Cs_2Ag_{0.40}Na_{0.60}InCl_6$:Bi–$SiO_2$.[45] Copyright 2021 Royal Society of Chemistry. (i) Emission spectra of $Cs_2Ag_{1-x}Na_xInCl_6$:Bi ($x$ = 0, 0.2, 0.4, 0.6, 0.8, 1).[14] Copyright 2021 Electrochemical Society.

### 3D LFMHPs

In 2014, Felix Deschler *et al.*[25] prepared methylammonium iodide ($CH_3NH_3I$) by a solvent evaporation method, and then dissolved $CH_3NH_3I$ and lead(II) chloride ($PbCl_2$) in anhydrous *N*,*N*′-dimethylformamide at a 3 : 1 molar ratio. $CH_3NH_3PbI_{3-x}Cl_x$ thin films were prepared by spin-coating from a precursor solution. The photoluminescence (PL) observed from $CH_3NH_3PbI_{3-x}Cl_x$ thin films are mainly attributed to recombination of free charges (electron and hole) within the films. At room temperature, free charges are formed under 1 ps photoexcitation and exhibit a long lifetime, resulting in very efficient PL with a high PLQY of 70%. This reveals the potential of 3D perovskite semiconductors in emission applications due to their facile processing and high luminous efficiency. Additionally, Protesescu *et al.* have opened a new avenue for the development of MHPs by designing highly efficient perovskite colloidal quantum dots (QDs).[50] They synthesized $CsPbX_3$ QDs using a simple preparation method and the emission of the prepared perovskites was in the visible region of 410–700 nm with PLQYs up to 90%, indicating tunable bandgap values of MHPs. It can be seen that photoelectronic performance of QDs is better than that of thin films, and their enhanced PLQYs and stabilities enable them to be applied in PeLEDs.

Subsequently, Jellicoe *et al.* reported nontoxic LFMHP $CsSnX_3$ nanocrystals (NCs), which were synthesized by a hot-injection method.[41] As demonstrated in Fig. 2b, the prepared $CsSnX_3$ NCs possess a compact cubic structure. With the change of halogen in $CsSnX_3$ NCs, their optical spectra were found to extend from the visible-light range to the near-infrared (NIR) region (Fig. 2c). Owing to similar atomic sizes and orbital structures of $Sn^{2+}$ ions with those of $Pb^{2+}$ ions, Sn-based LFMHPs exhibit ideal 3D perovskite structures, but the measured PLQYs of $CsSnX_3$ are below 1%, which results from the existence of high-density defects. It has been found that the defect formation energy in Sn-based perovskites is as low as 250 meV, which leads to defect densities of up to $\sim 10^{19}$ $cm^{-3}$. Due to excellent stabilities and photoelectronic properties of three-dimensional lead-free double perovskites, they have attracted the attention of a large number of researchers. The density functional theory (DFT) results show that their stabilities can be evaluated with proper $t$ (tolerance factor) and $\mu$ (octahedral factor) values ($0.813 < t < 1.107$, $0.337 < \mu < 0.895$),[51] indicating 3D structures and good photoelectronic performance of lead-free double perovskites. For example, $Cs_2AgBiBr_6$ and $Cs_2AgInCl_6$ were characterized and found to possess 3D structures, in which $Ag^+$ and $Bi^{3+}$ ($In^{3+}$) together replace a pair of adjacent $B^{2+}$ ions and then form two octahedrons with halogens, as demonstrated in Fig. 2d. In 2018, Zhou *et al.* prepared $Cs_2AgBiBr_6$ double perovskite NCs by the hot-injection method, and their structure is shown in Fig. 2e. $Cs_2AgBiBr_6$ NCs possess good photoelectronic properties and stabilities under high temperature and humidity. However, it has been reported that most double perovskites exhibit indirect band structures, resulting in weak PL performance.[43] In addition, a series of $Cs_2AgBiX_6$ NCs composed of different halogens were prepared by an ion exchange method. Sidney E. *et al.* prepared $Cs_2AgBiX_6$ (X = Cl, Br) NCs by the hot-injection method. The synthesis and conversion diagram of $Cs_2AgBiX_6$ NCs in Fig. 2f further demonstrates that $Cs_2AgBiI_6$ can be synthesized by an anion exchange reaction. The product maintains the symmetry of cubic *Fm*3*m* with the structure of $CsAgBiBr_6$.[42] During the ion exchange process, the spectral characteristics of larger-size NCs illustrate their broadband emission with low-energy shifts, as well as an adjusted emission range in the 350–600 nm region. Furthermore, Yang *et al.* measured the carrier dynamics of double perovskite nanocrystals using time-resolved PL and femtosecond (fs) transient absorption (TA) spectroscopies, and found that the double perovskite NCs show an obvious sub-band-gap capture process, which originates from surface defects. To solve this problem, they used the surfactant oleic acid (OA) as ligands to passivate the defects, increasing the PLQY by 100 times. Even so, the PLQY is only 6.7%.[52] Li *et al.* proposed the $Al^{3+}$ doping strategy to change an indirect band gap of $Cs_2AgBiX_6$ into a direct band gap, thus enhancing its PL performance. As a result, its PLQY was improved to 17.2% and white LEDs with a CRI of 81 were fabricated by integrating $Cs_2AgBiX_6$ with $K_3SbCl_6$ on 365 nm UV chips.[53]

Among reported lead-free double perovskites, $Cs_2AgInCl_6$ has the characteristics of a direct band gap. Locardi *et al.* synthesized intrinsic double perovskite $Cs_2AgInCl_6$ NCs by using a colloidal method. They are stable in air and exhibit broadband white-light emission. The PL emission intensity of Mn-doped $Cs_2AgInCl_6$ NCs increases as the Mn doping

concentration increases from 0.5% to 1.5%, and the highest PLQY achieved was 16 ± 4%.[54] In order to better understand the mechanism of the doping strategy, Liao *et al.* doped $Cu^{2+}$, $Zn^{2+}$ and $Cd^{2+}$ ions into $Cs_2AgInCl_6$ NCs, and the subsequent band gap values were 2.21 eV, 2.22 eV and 2.30 eV, respectively. The influence of different dopants on direct gaps shows that metal dopants enable the band gaps in $Cs_2AgInCl_6$ to be changed (Fig. 2g).[44]

In 2021, Li *et al.* synthesized $Bi^{3+}$-doped $Cs_2Ag_xNa_{1-x}InCl_6$ QDs by the hot-injection method. Based on the broadband spectrum originating from self-trapped excitons in $Bi^{3+}$-doped $Cs_2Ag_xNa_{1-x}InCl_6$, they obtained excellent white light emission. The best PLQY of $Cs_2Ag_xNa_{1-x}InCl_6$ was achieved by doping a small amount of $Bi^{3+}$ ions. The PLQY increased to 57.3%, and the emission peak at 600 nm was obvious. The Na-alloy and Bi-doped $Cs_2Ag_xNa_{1-x}InCl_6$ QDs possess the same cubic structure as $Cs_2AgInCl_6$. The stability of the QDs was further improved by preparing $Cs_2Ag_xNa_{1-x}InCl_6$:Bi–$SiO_2$ thin films using perhydropolysilazane as the coating precursor, which was confirmed from Fig. 2h. XRD patterns of the $Cs_2Ag_{0.40}Na_{0.60}InCl_6$:Bi–$SiO_2$ thin films exhibited dominant peaks of $SiO_2$ and $Cs_2Ag_{0.40}Na_{0.60}InCl_6$ QDs. Compared with $Cs_2Ag_{0.40}Na_{0.60}InCl_6$:Bi QDs at room temperature, they exhibited nearly all the main diffraction peaks, therefore the temperature change did not cause a phase transition of the QDs, and it could be concluded that $SiO_2$ plays a protective role and thus prevented the phase transition of the QDs. It is known that coating passivation can inhibit surface-related non-radiative processes and PL intensity is improved after sufficient coating. In addition, after heat treatment at 200 °C, the PL intensity of the film based on coating QDs is enhanced, and its PLQY is higher than that of uncoated QDs.[45] Subsequently, Wang *et al.* studied the phase structures, morphologies and luminescence properties of $Cs_2Ag_{1-x}Na_xInCl_6$:Bi with different Na contents. $Cs_2Ag_{1-x}Na_xInCl_6$:Bi has a wide emission peak at 600 nm, as shown in Fig. 2i. When $x = 0.8$, its PLQY reaches 86.91%, which has been identified as the best value among reported double perovskites.[14]

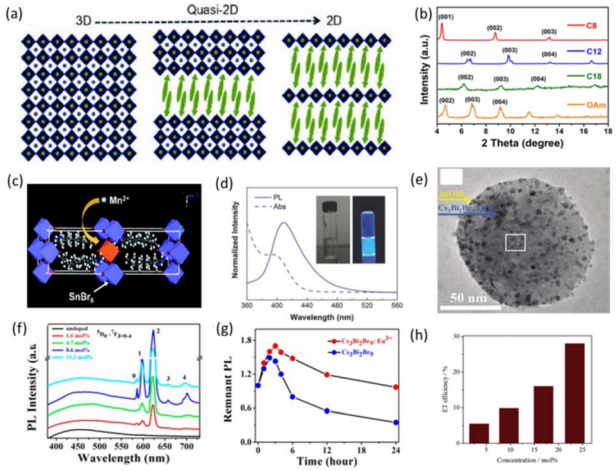


Fig. 3 (a) Perovskite lattices with different dimensions ($n = \infty$, 3D structure; $n = 1$, pure 2D structure; and $n$ = defined integer, quasi-2D structure).[55] Copyright 2014 Wiley-VCH. (b) XRD patterns for tin-based perovskites.[56] Copyright 2019 American Chemical Society. (c) Schematic representation of 2D single-layered $(C_8H_{17}NH_2)_2Sn_{1-x}Mn_xBr_4$ ($x = 0.25$).[57] Copyright 2020 Royal Society of Chemistry. (d) Absorption and PL spectra of $Cs_3Bi_2Br_9$ QD synthesis. Insets: typical optical images of the QD solution in ambient light and under 325 nm UV lamp illumination.[58] Copyright 2017 Wiley-VCH. (e) TEM images of the water-induced $Cs_3Bi_2Br_9$/BiOBr nanocomposites.[59] Copyright 2020 Royal Society of Chemistry. (f) Emission spectra of undoped and $Eu^{3+}$ ions-doped $Cs_3Bi_2Br_9$ QDs with different doping concentrations.[60] Copyright 2019 American Chemical Society. (g) PL intensity of undoped and $Eu^{3+}$ ions-doped $Cs_3Bi_2Br_9$ PeQDs as a function of time in water.[60] Copyright 2019 American Chemical Society. (h) Energy transfer efficiency from PQDs to $Sm^{3+}$ *versus* $Sm^{3+}$ doping concentrations.[61] Copyright 2020 Chinese Society of Rare Earths.

## 2D LFMHPs

Recently, researchers have used long-chain alkylammonium ions to separate 3D octahedra, with adjacent layers stacked on top of each other by van der Waals forces between organic chains. As shown in Fig. 3a, long hydrophobic chains provide 2D perovskites with better moisture resistance and thermal stability than 3D perovskites. Wang *et al.* reported emissive 2D (OCTAm) $_2SnX_4$ (OCTAm = octylammonium cation) LFMHPs with a near-unity PLQY and ultrahigh stability in acidic aqueous solutions.[62] Hou *et al.* reported that different carbon chains can affect the photoelectronic effect of 2D tin-based perovskites. They reported the synthesis of 2D LFMHPs by selecting different long-chain amines ($RNH_2$), as shown in Fig. 3b. $(C_8H_{17}NH_2)_2SnBr_4$ (PLQY = 54%), $(C_{12}H_{25}NH_2)_2SnBr_4$ and $(C_{18}H_{37}NH_2)_2SnBr_4$ (PLQY = 2%) emit bright yellow light (~615 nm), and $(OAm)_2SnBr_4$ (PLQY = 60%) emits excellent orange light (~628 nm). This also proves that organic carbon chains have an effect on the properties, in which the flexibility of the carbon chains influences the arrangement of the carbon chains and the distortion of the octahedral layers. As a result, changes in binding energy, which are attributed to the arrangement of the carbon chains and distortion of the $[SnBr_6]^{4-}$ octahedra, affect the band gap of tin-based LFMHPs.[56] Hou *et al.* found that the energy level of a Mn $^4T_1$ orbital was close to that of the self-induced exciton, which could effectively reduce the energy loss during the energy transfer process. Therefore, they doped 2D Sn-based perovskites with Mn ions through a solid grinding method. The structure of the prepared $(C_8H_{17}NH_2)_2Sn_{1-x}Mn_xBr_4$ is shown in Fig. 3c. Its emitted light is orange and red, and originates due to the emission of self-trapped excitons (STEs) from the host crystal and the effective emission of the d–d orbital transition ($^4T_1$–$^6A_1$) in Mn ions. However, the prepared LFMHPs exhibit PL as a single broad band due to the competition between STEs and the doped Mn d–d transition emission.[57] In order to explore the broadband emission of STEs from a 2D lead-free perovskite, Li *et al.* synthesized Sn-based perovskites of $R_{2+x}SnI_{4+x}$, which has broadband emission with the highest PLQY reaching 99%. Its stability and good photoelectronic performance make it suitable for potential application in solid-state lighting.[63]

In addition, other $A_3B_2X_9$ (B = Bi, Sb) LFMHPs exhibit a 2D layered structure. Leng *et al.* synthesized 2D $Cs_3Bi_2Br_9$ QDs with blue light emission using a modified ligand-assisted

recrystallization method. Absorption and PL spectra of $Cs_3Bi_2Br_9$ QDs are shown in Fig. 3d. In the PL spectrum, an emission peak is observed at 410 nm with a FWHM of 48 nm and a PLQY of ~19.4%. Compared with single crystals, the PL peak of QDs shows a blue shift of 60 nm, indicating a strong quantum confinement effect. In addition, colloidal $Cs_3Bi_2Br_9$ quantum dots exhibit good stability when exposed to water due to the formation of self-passivation layers of BiOBr.[58] Based on the water stability of $Cs_3Bi_2Br_9$ QDs, Ma *et al.* proposed a strategy to improve the PLQY of $Cs_3Bi_2X_9$ QDs by using water-induced nanocomposites. The QDs are encapsulated in a BiOBr matrix. By optimizing the water treatment in $Cs_3Bi_2Br_9$ QDs, as shown in Fig. 3e, $Cs_3Bi_2Br_9$ QDs were encapsulated into the BiOBr matrix, which led to an enhancement of their PLQY by approximately 130% (from 20.2% to 46.4%) and improved color purity.[59] The low PLQY of $Cs_3Bi_2Br_9$ QDs can be attributed to the intrinsic surface defects, and the lattice defects of $Cs_3Bi_2Br_9$ can be reduced by the doping strategy, allowing doping ions to occupy defect states. Ding *et al.* doped $Eu^{3+}$ ions into $Cs_3Bi_2Br_9$ QDs, which demonstrated an increased PLQY of 42.4% and multicolor emission using an improved ligand-assisted reprecipitation method. As shown in Fig. 3f, the ratio of PL intensity between $Eu^{3+}$ ion emission and exciton emission increases with increasing $Eu^{3+}$ doping concentration, which implies a higher effective energy transfer (ET) from $Cs_3Bi_2Br_9$ QDs host to the $Eu^{3+}$ ion level. However, with the further increase of $Eu^{3+}$ doping concentration, a self-quenching process occurs among the $Eu^{3+}$ ions, resulting in the reduction of PL intensity of the $Eu^{3+}$ ions. As shown in Fig. 3g, $Eu^{3+}$-doped $Cs_3Bi_2Br_9$ QDs exhibit better stability in water than undoped $Cs_3Bi_2Br$ QDs.[60] Zhu *et al.* also doped $Sm^{3+}$ ions into $Cs_3Bi_2Br_9$ QDs using an improved ligand-assisted recrystallization method. The PLQY of $Cs_3Bi_2Br_9$ QDs increased from 10.9% to 20.8%, and the water resistance stability also significantly improved. As shown in Fig. 3h, the efficiency of ET increases with the increase of $Sm^{3+}$ dopant concentration, indicating that doping is an effective method to improve the PLQYs of LFMHPs.[61]

### 1D LFMHPs

$BX_6$ octahedra of 1D perovskites are linked in chains (corner-, side-, and face-sharing) and surrounded by organic cations. In 2017, Zhou *et al.* prepared the 1D-structure of $C_4N_2H_{14}SnBr_4$ from a hydrothermal reaction of equal amounts of $SnBr_2$ and $C_4H_{14}N_2Br_2$ in a mixture of 48% w/w hydrobromic acid (HBr) and 50% w/w hypochromic acid ($H_3PO_2$) aqueous solution, where $H_3PO_2$ can prevent the oxidation of $Sn^{2+}$ ions. As shown in Fig. 4a, 1D $C_4N_2H_{14}SnBr_4$ has a similar structure to $C_4N_2H_{14}PbBr_4$, where the metal halide chains of $[SnBr_4]^{2-}$ are surrounded by $C_4N_2H_{14}{}^{2+}$ cations. However, unlike the intense white light emission observed in 1D lead bromide perovskite ($C_4N_2H_{14}PbBr_4$), 1D $C_4N_2H_{14}SnBr_6$ does not emit white light because the size of Sn is smaller than Pb, leading to structural distortion and suppressed recombination of excitons in 1D $C_4N_2H_{14}SnBr_6$.[64] In terms of Mn-based LFMHPs, because of the $3d^5$ structure in Mn ions, the luminescence changes of Mn vary greatly under different crystal field environments. Mn ions

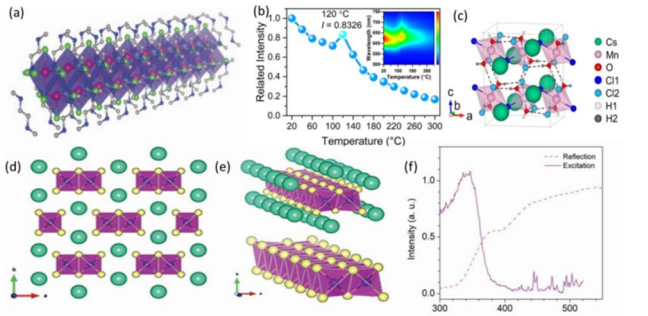


Fig. 4 (a) Views of a 1D Sn bromide wire wrapped by organic cations.[64] Copyright 2017 Wiley-VCH. (b) The variation in the integrated emission intensity ($\lambda_{ex}$ = 416 nm) of $CsMnCl_3(H_2O)_2$ *vs.* the heating temperature (20–300 °C). Inset in the upper right shows the temperature-dependent PL spectra of $CsMnCl_3(H_2O)_2$.[65] Copyright 2020 Wiley-VCH. (c) Crystal structure of $CsMnCl_3(H_2O)_2$, hydrogen bonds (O–H) depicted as black dashed lines.[65] Copyright 2020 Wiley-VCH. (d) Structure of 1D $CsCu_2I_3$ SC (green: Cs atom, yellow: I atom, dark blue: Cu atom, purple octahedron: Cu–I octahedron).[66] Copyright 2019 Wiley-VCH. (e) Cu–I 1D chain surrounded by Cs atoms and the independent Cu–I chain that is likea "nanowire".[66] Copyright 2019 Wiley-VCH. (f) Ultraviolet excitation spectrum collected at 568 nm and reflection spectrum.[66] Copyright 2019 Wiley-VCH.

enable green light emission in weak fields, and orange to red light emission in strong fields, which also has a positive effect on the luminescence efficiency in low-dimensional perovskites.[67] Xiao *et al.* prepared 1D $CsMnCl_3(H_2O)_2$ single crystals using a typical crystallization method, and mixed isomolar $MnCl_2(H_2O)_4$ and CsCl in concentrated hydrochloric acid at 80 °C. After cooling and crystallization, pink single crystals of $CsMnCl_3(H_2O)_2$ were obtained, which emit red light under ultraviolet (UV) excitation. The 1D crystal structure of $CsMnCl_3(H_2O)_2$ is shown in Fig. 4c. Each $Mn^{2+}$ ion is coordinated with four $Cl^-$ ions and two $O^{2-}$ ions to form a twisted $[MnCl_4(H_2O)_2]^{2-}$ octahedron, which is connected by a common vertex to form a zigzag chain. In addition, each $Cs^+$ ion is surrounded by eight nearest $Cl^-$ ions, thus connecting the octahedra. They measured temperature-dependent PL spectra from 20 to 300 °C, as shown in Fig. 4b. The PL intensity initial decreased to 100 °C and slightly increased at 120 °C, then decreased again. This was attributed to the loss of crystal water. Compared with $CsMnCl_3(H_2O)_2$, the PLQY of $CsMnCl_3$ increases from 13% to 36%, which is due to the strong coupling of excitons with tensile vibration of $OH^-$ groups, which eliminates nonradioactive recombination and quenching fluorescence.[65] Pandurangan *et al.* adopted simple ultra-sonication and the modified ligand-assisted reprecipitation method to prepare 1D lead-free Mn halide NCs in methanol instead of DMF, so that the synthesized Mn-based perovskites are highly stable.[68]

A new type of $Cu^+$-based LFMHP has attracted the extensive attention of researchers. Taking $CsCu_2I_3$ as an example, it possesses a typical 1D structure on the molecular level.[69] Huang *et al.* successfully prepared 1D $CsCu_2I_3$ SCs by dropping methanol into the mixture of saturated solutions (dimethyl sulfoxide (DMSO) and dimethyl formamide (DMF) at a ratio of 1 : 4, and dissolved a certain proportion of CsI and CuI) through the

antisolvent impregnation method. The 1D crystal structure of $CsCu_2I_3$ with isolated $[Cu_2I_3]^-$ chains in the second-dimension direction is shown in Fig. 4d and e. The emission spectra at room temperature are shown in Fig. 4f. The strong absorption peak is located at 328 nm, the optical band gap is measured as 3.78 eV, and a Stokes shift of 1.51 eV is found, indicating recombination of self-trapped excitons.[66] Shi *et al.* dissolved different proportions of CsI and CuI in γ-butyrolactone through a rapid antisolvent crystallization process with isopropanol. After stirring the solution at 80 °C for 2 hours, the mixture was cooled naturally to room temperature. Then the supernatant of the mixture was quickly injected into isopropyl alcohol (10 mL) and stirred vigorously in the air at room temperature, producing white $Cs_3Cu_2I_5$ and $CsCu_2I_3$ precipitates immediately. Under UV excitation, blue and yellow light was emitted, respectively. The PL spectra cover almost the entire visible range of 370–750 nm. By evaluating the absorption spectra of the two products, the optical band gap of 0D $Cs_3Cu_2I_5$ is 3.78 eV, and that of 1D $CsCu_2I_3$ is smaller than 4.11 eV. Therefore, larger Stokes shifts indicate that Cu-based perovskites with a 1D structure have greater lattice distortion. The two compounds can be converted into each other by a mechanochemical reaction. Thus, standard white light emission can be obtained from the mixture of these two compounds in appropriate proportions, showing good optical properties.[70]

### 0D LFMHPs

In 0D LFMHPs, the structures of the metal halide polyhedra are independent and not connected to the surrounding cations. As a result, a flat band structure is formed, which effectively inhibits photoexcitons, leading to the emission of strong excitons and significantly promoting radiation recombination.[74] Under excitation, independent 0D structures cause lattice deformation to produce self-trapped exciton (STE) emission, thus achieving efficient luminescence. In recent years, a large number of lead-free perovskite compounds with 0D structures have been explored and synthesized, and their highly tunable emission and remarkable PLQYs have attracted the attention of many researchers.[75] In 2018, Kovalenko *et al.* used a simple solid-state heating approach to heat a mixture of CsBr and $SnBr_2$ at 350 °C for 60 hours. In this process, $Cs_4SnX_6$ NCs were ground in a glove box and prepared by annealing. As shown in Fig. 5a, the crystallization of $Cs_4SnX_6$ belongs to a trigonal crystal system, forming an *R3c* space group, where $Cs^+$ ions occupy two different crystal positions and separate $[SnBr_6]^{4-}$ octahedra.[4] Compared with the $CsSnBr_3$ perovskite, $Cs_4SnBr_6$ shows excellent stability in air.[41] In addition, they prepared $Cs_{4-x}A_xSn(Br_{1-y}I_y)_6$ (A = Rb, K; $x \leq 1$, $y \leq 1$), which exhibits 500–620 nm broadband emission. As shown in Fig. 5b, both broadband emission and long radiation lifetime indicated the formation of STEs. Zhang *et al.* reported a simple room-temperature antisolvent synthesis of lead-free green-light-emitting $Cs_4SnBr_6$ (~524 nm) and cyan-green-light-emitting $Cs_3KSnBr_6$ (~500 nm) with 0D structures. By evaluating the PL, PLE and absorption spectra of $Cs_4SnBr_6$ and $Cs_3KSnBr_6$ (Fig. 5c and d), large FWHM values greater than 100 nm were

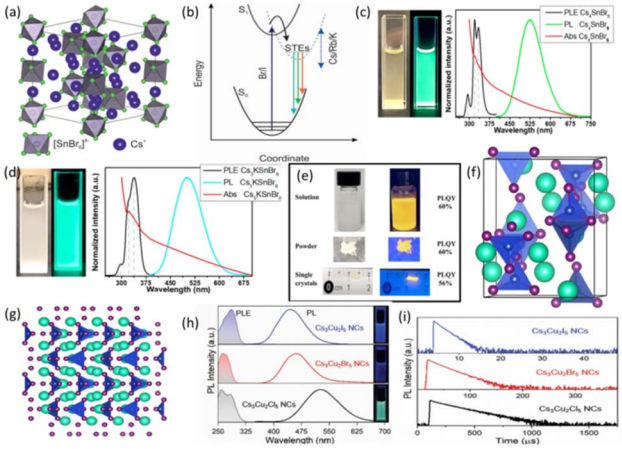


Fig. 5 (a) The crystal structure of $Cs_4SnBr_6$ viewed along the (111) axis with $[SnBr_6]^{4-}$ octahedra (gray with green bromine atoms) separated by $Cs^+$ cations (blue).[4] Copyright 2018 Wiley-VCH. (b) Configurational coordinate diagram illustrating the origin of STE PL in $Cs_{4-x}A_xSn(Br_{1-y}I_y)_6$.[4] Copyright 2018 Wiley-VCH. PL, PLE, and Abs of (c) $Cs_4SnBr_6$ and (d) $Cs_3KSnBr_6$ perovskites. Photographs of colloidal NCs captured under daylight and 302 nm UV light, respectively.[30] Copyright 2020 American Chemical Society. (e) Photographs of $[Na(DMSO)_2]_3SbBr_6$ solution, powder, and single crystals with/without UV light.[71] Copyright 2022 Wiley-VCH. (f) and (g) Crystal structure of $Cs_3Cu_2I_5$.[72] Copyright 2018 Wiley-VCH. (h) PLE and PL spectra of colloidal $Cs_3Cu_2X_5$ NC solutions in hexane. Right insets show photographs of $Cs_3Cu_2X_5$ NC solutions under UV lamp excitation with $\lambda$ = 254 nm.[73] Copyright 2019 Wiley-VCH. (i) Time-resolved PL decay spectra of $Cs_3Cu_2X_5$ NC solutions.[73] Copyright 2019 Wiley-VCH.

measured, which is desirable, indicating the existence of a strong phonon–electron coupling effect.[30] In addition, Stokes shifts were found to decrease from 204 nm ($Cs_4SnBr_6$) to 180 nm ($Cs_3KSnBr_6$). It may be attributed to changes in the Jahn–Teller distortion in the Sn–Br octahedra, where the elongation of axial Sn–Br bonds and the contraction of the equatorial Sn–Br bonds are included.[4] However, the air stability of Sn-based 0D LFMHPs was not greatly improved, which may be due to oxidation of $Sn^{2+}$ ions in the air. Thus, it is urgent to explore 0D LFMHPs with high-valence lead-free metal ions. 0D $[Na(DMSO)_2]_3SbBr_6$ NCs were synthesized by Zang *et al.* using the antisolvent strategy under standard atmospheric conditions, in which toluene acted as the antisolvent. During the preparation process, the precursor solution was obtained by dissolving NaBr and $SbBr_3$ into DMSO. Isolated $[SbBr_6]^{4-}$ octahedra are surrounded by $[Na(DMSO)_2]_3$, and the prepared NCs exhibit bright broadband yellow-light emission under UV light excitation.[71] The photoluminescence of $[Na(DMSO)_2]_3SbBr_6$ is regarded as originating from STEs, and its colloidal solution, powders and single crystals exhibit high PLQYs of 60%, 60%, and 56%, respectively, as shown in Fig. 5e.

$Cs_3Cu_2X_5$ (X = Cl, Br, I), with a formula of $A_3B_2X_5$, is one of the representative 0D LFMHPs in which there are two polyhedra (triangular planes $[CuI_3]^{2-}$ and $[CuI_4]^{3-}$), as shown in Fig. 5f and g. The unique 0D structure results in the presence of strong local electrons.[51] In 2018, Hosono *et al.* synthesized a $Cs_3Cu_2I_5$ single crystal with a size of about 5 mm using a solvent-resistant

steam saturation method. Strong blue PL was observed at 445 nm and the PLQY reached 90%. A single-crystal $Cs_3Cu_2I_5$ thin film was successfully prepared that possesses bright blue PL with a high PLQY of 62% at room temperature, and the PLQY was almost unchanged after being stored for two months, while the PLQY in the QD film suffered from PLQY degradation, which was attributed to the aggregation of QDs.[72] Wu *et al.* utilized a vacuum dual-source thermal deposition strategy to prepare $Cs_3Cu_2I_5$ thin films, which were directly deposited on a hot quartz substrate with a CsI/CuI molar ratio of 3 : 2. Annealing treatment was applied to the films in the deposition process, thus their crystals began to grow when precursors were attached to the substrate, avoiding the incomplete reaction of precursors and optimizing the morphologies of the $Cs_3Cu_2I_5$ thin films.[76] In order to explore the tunable broadband emission of $Cs_3Cu_2X_5$ NCs, Quan *et al.* synthesized $Cs_3Cu_2X_5$ using the hot-injection method. As shown in Fig. 5h, the PLE and PL spectra of $Cs_3Cu_2X_5$ (X = I, Br, and Cl) NCs show clear exciton characteristics, and the emission peaks of the $Cs_3Cu_2X_5$ NCs change from 445 to 527 nm, which can be attributed to STE emission. Fig. 5i shows the transient PL spectra of $Cs_3Cu_2I_5$ NCs with a different halogen. The long lifetime of $Cs_3Cu_2X_5$ NCs is 1.56 μs (X = I), 14.12 μs (X = Br), and 135.97 μs (X = Cl). In addition, $Cs_3Cu_2I_5$ NCs exhibit excellent PL stability over 45 days, while PL quenching is found in $Cs_3Cu_2Br_5$ and $Cs_3Cu_2Cl_5$ due to oxidation.[73] During the preparation of $Cs_3Cu_2X_5$ NCs, the purity of the products was difficult to enhance. To solve this problem, Zang *et al.* prepared $Cs_3Cu_2Cl_3$ and $Cs_3Cu_2Cl_5$ NCs emitting bright blue and green light, respectively, by controlling the reaction temperature (70 °C and 120 °C) during the hot-injection process. The PLQY of $Cs_3Cu_2I_5$ was up to 87.2% and the emission spectrum was broadband. The results show that the reaction temperature can determine the final composition of Cu-based LFMHPs.[77]

## The preparation methods of LFMHP materials

It is known that LFMHPs can be divided into 0D, 1D, 2D and 3D structures according to their atomic arrangement order, and they can also be divided into films, single crystals, powders and NCs according to their morphologies and composition.[78] Owing to the diverse crystal configuration and low formation energy of LFMHPs, various preparation methods, such as the antisolvent reprecipitation method,[71] the hot-injection method,[79] and the solvent thermal method,[80] have been proposed and developed to prepare LFMHPs. Different preparation methods have an impact on the characteristics and structures of the LFMHPs, as well as affect their optoelectronic performance.[81–89] As a result, the preparation methods can determine the manufacture and performance of perovskite LEDs (PeLEDs).

### Antisolvent-induced reprecipitation method

During the antisolvent reprecipitation method, the solubility of the solvent is reduced due to the introduction of antisolvent-induced reprecipitation into the solution. In general, according to the polarity and electrolytic capacity of the solvent, an organic solvent can be divided into good solvents (high solubility of precursors in given solvents) and weak solvents (low solubility of precursors in given solvents). Among them, good solvents, including dimethyl sulfoxide (DMSO), *N*,*N*-dimethylformamide (DMF), gamma-hydroxybutyrolactone (GBL) and dichloromethane (DCM), generally have a high polarity, which can dissolve highly ionic precursors. The polarity of weak solvents is weak or even non-polar, thus it is difficult for them dissolve some highly ionic precursors. Examples of weak solvents include toluene, chlorobenzene, ether, methanol and *n*-octane.[18] As shown in Fig. 6a, during the antisolvent-assisted crystallization process, mixed precursors can be dissolved efficiently in a good solvent, and it is well known that a mixture of a weak solvent and a good solvent is completely immiscible. A weak solvent enables the content of a good solvent in a precursor solution to be continuously consumed during the diffusion process, resulting in a decrease of solubility and the achievement of saturation states. As a result, precipitate of LFMHP single crystals can be obtained from solution.[90] The decreased rate of solubility determines the precipitation rate of single crystals. This method is relatively simple and facile, and there are many kinds of solvent and antisolvent.[52]

As shown in Fig. 6b, Fang *et al.* synthesized a CsI–CuI solution using the antisolvent reprecipitation method,[70] and the resulting $CsCu_2I_3$ single crystals were filtered and washed

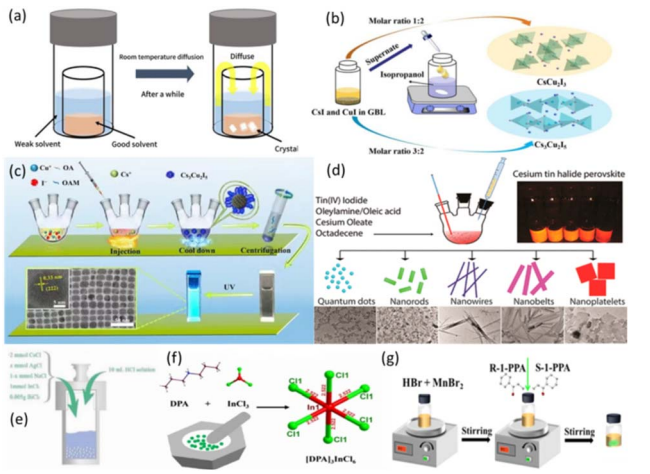


Fig. 6 (a) Diagram of antisolvent-assisted crystallization.[90] Copyright 2020 Elsevier Ltd. (b) Schematic illustration of the synthetic process for cesium copper iodide with different stoichiometric ratios.[70] Copyright 2012 Royal Society of Chemistry. (c) Schematic diagram for the colloidal synthesis of blue-light-emitting $Cs_3Cu_2I_5$ NCs.[79] Copyright 2020 American Chemical Society. (d) Schematic diagram of controlled synthesis procedure of perovskite $Cs_2SnI_6$ NCs (left) and photo of prepared $Cs_2SnI_6$ sample under UV light (right).[91] Copyright 2016 American Chemical Society. (e) Diagram of preparation of perovskites by a hydrothermal method.[14] Copyright 2021 Electrochemical Society. (f) Mechanochemical grinding solid state preparation method, and $[InCl_6]^{3-}$ unit structure of $[DPA]_3InCl_6$.[92] Copyright 2021 Chinese Chemical Society. (g) The experimental operation step diagram of preparation of $(R/S\text{-1-PPA})_2MnBr_4$.[93] Copyright 2022 Elsevier B.V.

thoroughly with isopropyl alcohol. Finally, $CsCu_2I_3$ single crystals exhibited strong yellow-light emission with a FWHM of ~120 nm under 305 nm UV excitation. However, when the molar ratio of CsI to CuI is changed to 3 : 2, the resulting precipitate is regarded as $Cs_3Cu_2I_5$, which shows emission of blue light with a FWHM of ~82 nm under UV excitation. When the molar ratio is 1 : 1, there are both $CsCu_2I_3$ and $CsCu_2I_5$ in the precipitate. The luminescence spectra of $Cs_3Cu_2I_5$ and $CsCu_2I_3$ show strong and broadband emission, which almost covers the whole visible spectrum range of 370–750 nm.

Another common strategy for preparing LFMHPs is the co-precipitation crystallization method, which is commonly used for growing single crystals. In 2021, Chen *et al.* reported the synthesis of $Cs_2ZrCl_6$ single crystals with the assistance of concentrated hydrochloric acid *via* a simple co-precipitation method, where CsCl, $ZrOCl\cdot 8H_2O$, $SbCl_3$ and 37% hydrochloric acid (HCl) were the raw materials. $Cs_2Zr_{1-x}Cl_6{:}xSb^{3+}$ ($x$ = 1, 5, 10, 20%) single crystals were obtained from different molar ratios of $SbCl_3$ and $ZrOCl\cdot 8H_2O$, and they showed different PL performance. It was found that intrinsic $Cs_2ZrCl_6$ shows blue-light STE emission centered at 445 nm under 260 nm excitation, and the FWHM is 135 nm. $Cs_2ZrCl_6$ doped with 10% $Sb^{3+}$ shows the strongest broadband blue-light emission peaks at 495 nm and red-light emission peaks at 622 nm with a PLQY of about 78%.[29] $Sb^{3+}$ doping was proved to facilitate the strong electron–phonon coupling in the soft crystal structure, leading to the formation of STEs.

Although the antisolvent reprecipitation method is an effective method for preparing MHPs, the antisolvent-assisted crystallization method shows a high selectivity for organic solvents with low solubility. In addition, during the synthesis process, the fast diffusion rate of a weak solvent may cause fast crystallinity, resulting in the production of metal-halide powders instead of single crystals. In comparison, the slow diffusion rate of a solvent has been found to affect the crystal quality of LFMHP single crystals.[58] Furthermore, the single-crystal growth period is slow in this process, and the crystallization process is uncontrollable, so the antisolvent-assisted crystallization method is not suitable for fabricating large-size single crystals.[30,70,94]

### Hot-injection method

Hot injection is a rapid preparation method, in which a precursor solution is injected into a hot solution containing ligands at a high temperature (usually above 120 °C).[95] Due to its fast injection speed, when the reaction solution is saturated, fast nucleation and growth occur immediately, facilitating dispersal of the final product in solution. This synthesis method can be used to synthesize small, monodisperse and high-crystallinity NCs. The sizes, distribution, and shapes of the NCs depend on the ratios of surfactants to precursors, as well as the concentration of precursor, injection temperature, and reaction time.[79] As shown in Fig. 6c, Wang *et al.* synthesized $Cs_3Cu_2I_5$ NCs using a modified hot-injection method. The synthesis process can be described simply as dissolving copper iodide precursors into cesium oleate, and cooling the mixture after a short reaction time. $Cu^+$ ions combine with $Cs^+$ and $I^-$ ions to form $Cs_3Cu_2I_5$ NCs stabilized by oleic acid (OA) and octylamine (OAM) ligands. Under excitation of UV light, the colloidal solution of NCs shows bright blue-light emission at 445 nm with a FWHM of 63 nm and a PLQY of 87%, as well as negligible PL degradation of $Cs_3Cu_2I_5$.[91] Cesium oleate and tin iodide(IV) act as precursors in the solution containing OA and OAm. Even after exposure of the cesium oleate $Cs_3Cu_2I_5$ to an air environment for 35 days, its stability against water and oxygen was maintained.[79]

Wang *et al.* synthesized well-structured lead-free and stable $Cs_2SnI_6$ NCs with different morphologies by the simple hot-injection method, as shown in Fig. 6d.[91] White products were observed at first, which then turned dark-brown. The crude solution was then purified with a mixture of toluene and hexane (1/1 v/v) under ambient conditions. Finally, the NCs were dried in a bottle. When adjusting the reaction temperature and time, as well as the ratios of precursors, spherical QDs, nanorods, nanowires and nanosheets of the synthesized $Cs_2SnI_6$ are obtained.

The hot-injection method is regarded as a common method in the preparation of LFMHPs. According to previous studies about LFMHPs, the hot-injection method is usually used for the synthesis of NCs[96] and QDs,[70] because this method can obtain more evenly distributed products. However, there is often solvent residue on the surface of the products, which has an impact on the performance of the prepared products.[94] Therefore, improving the solubility of the solvent and exploring new good solvents are required to optimize the hot-injection method.

### Solvent thermal method

A hydrothermal method refers to a chemical reaction in a sealed pressure vessel with water as the solvent under high temperature and pressure conditions. According to different reaction types, it can be divided into hydrothermal oxidation, reduction, precipitation, and crystallization. Among them, the hydrothermal crystallization method is the most commonly used, and its main principle is dissolution and recrystallization. Firstly, reactants are dissolved in a hydrothermal medium in a certain proportion, facilitating ionization in solution.[64] Then, the strong convection of the autoclaves enables transport of these ions to the low-temperature area, forming a saturated solution and crystallization of the precipitate. In terms of the solubility of various LFMHPs, the solvothermal method is beneficial for the preparation of LFMHPs with different structures.[97] Wang *et al.* prepared Bi-doped $Cs_2Ag_{1-x}Na_xInCl_6$ using the hydrothermal method,[14] in which a mixture of $InCl_3$, CsCl, AgCl, and a small amount of $BiCl_3$ were dissolved in hydrochloric acid solution, as shown in Fig. 6e. The solution was sealed in PTFE bottles and heated in an oven to 180 °C for 12 hours, and then cooled to 50 °C. It was found that the highest PLQY of 86.91% in Bi-doped $Cs_2Ag_{1-x}Na_xInCl_6$ was obtained when $x = 0.8$, and its PL spectrum was in the range of 400–780 nm. Jiang *et al.* also prepared $Cs_2NaBiCl_6$ (ref. 98) single crystals by the hydrothermal method, and studied the relationship between the

optical response and phase transition of $Cs_2NaBiCl_6$ under high pressure. Li *et al.* used the solvothermal method to synthesize all-inorganic lead-free perovskite $Cs_2Zr_{1-x}Te_xCl_6$ ($x$ = 0–0.3) microcrystals (MCs).[80] The prepared pure $Cs_2ZrCl_6$ MCs showed blue-light emission at 460 nm, while $Cs_2Zr_{1-x}Te_xCl_6$ perovskite MCs doped with $Fe^{4+}$ showed bright yellow-light emission with a PLQY up to 79.46% at room temperature.

The solvothermal method can not only be used with different solvents to obtain products with different structures, but also exhibits the advantages of simple processability, low-energy consumption, and controllable particle shapes.[99] However, the product yields of LFMHPs prepared from this method are low and their purities are not high enough.[100]

### Other methods

In addition to the methods described above, there are many other ways to prepare LFMHPs. Zhu *et al.* used a modified ligand-assisted recrystallization method[61] to dope $Sm^{3+}$ ions into $Cs_3Bi_2Br_9$ QDs, which then exhibited effective white-light emission. Two new crystalline hybrid indium chloride materials $[DAPEDA]InCl_6 \cdot Cl \cdot H_2O$ and $[DPA]_3InCl_6$ (DAPEDA = $C_8H_{22}N_4$, DPA = $C_6H_{15}N$) were prepared by Sun *et al.* using a facile wet-chemistry method, as shown in Fig. 6f,[92] and they exhibited strong broadband green-light emission with PLQY values of 40% and 34%, respectively. Zang *et al.* also used a solid mechanical grinding method to prepare 0D hybrid copper halide $(TMA)_3Cu_2Br_{5-x}Cl_x$ powders, which possess strong broadband emission and a PLQY up to 75%, as well as good stability to heat and air.[7] Wang *et al.* successfully prepared a pair of lead-free manganese halide enantiomers $(R/S\text{-1-PPA})_2MnBr_4$ ($R/S$-1-PPA = $R/S$-1-phenylpropane-1-amine) using a solution method, as shown in Fig. 6g.[93] However, its PLQY dropped sharply when the film was prepared.[101] Therefore, the preparation technology of LFMHPs needs to be further improved.

## WLEDs based on LFMHPs

In solid-state lighting, the white light of ideal light sources should be continuous and stable, and the chromaticity coordinate of ideal white light is (0.33, 0.33). Researchers often use a correlated color temperature (CCT), color rendering index (CRI), energy conversion efficiency (ECE), and lifetime to evaluate the luminous quality of white light. Various CCT values of light sources can cause different feelings to humans. CCT of warm white light is about 2700 K, neutral white light is about 4000 K, and when the CCT is above 5000 K, it is known as cold white light.[105] The CRI ranges from 0 to 100, and white light with a higher CRI enables the true color of objects to be illustrated.[106] ECE($\eta$) represents the energy conversion efficiency in lumens/watts and can be expressed by the formula: $\eta = \Phi_v/P_1$, where $\Phi_v$ is the total luminous flux (the energy radiated per unit of time from the source at the visible wavelength) and $P_1$ is the total lamp power input or radiant power emission.[107] The lifetime is defined as the time it takes for the brightness to decline to a specific percentage of its initial value.[108] Directly mixing lead-based perovskites does not lead to emission of white light due to an anion exchange reaction. Therefore, by mixing LFMHPs with other emitting materials, a reasonable device structure can be designed and fabricated to emit white light.[109] The white light produced by LFMHPs can be divided into two forms: (1) multiple LED chips or emitters of different colors are connected, and perovskite electroluminescence (EL) enables ideal white light through voltage and current excitation; (2) the LFMHPs can be activated by blue or UV chips to emit high-performance white light through photoluminescence (PL). In this section, a brief description on the development of WLEDs based on LFMHPs from these two aspects is given.

### Electroluminescent (EL) WLEDs based on LFMHPs

The main components of electroluminescent devices are luminescent layers; electron transport layers (ETLs), and hole transport layers (HTLs), as well as upper and lower electrodes. The two kinds of carrier recombination processes of electroluminescent devices are as follows: the first one is that electrons and holes are injected into the luminescent layer under a driving voltage, forming excitons to emit photons through radiation recombination. The second type is Förster resonance energy transfer, in which electrons or holes are not confined in the luminescent material layers, but in hole transport layers or electron transport layers, and then transferred to the luminescent layers through Förster resonance. Composite emission of photons then occurs in the luminescent layers. These two carrier recombination processes can exist simultaneously and have no influence on each other. Key indicators to evaluate an electroluminescent LED are the external quantum efficiency, current efficiency and opening voltage.

In 2018, Luo *et al.* reported a lead-free double perovskite $Cs_2(Ag_{0.60}Na_{0.40})InCl_6$ film that showed a high PLQY of 86%. Due to the existence of STEs, one-component warm white-light emission can be realized in $Cs_2(Ag_{0.60}Na_{0.40})InCl_6$. Fig. 7a shows the structure of the fabricated EL device, in which carrier injection and transport can be regulated in carrier transporting layers.[16] Under driving voltages, the EL device exhibits broadband emission, demonstrating a peak current efficiency of 0.11 cd $A^{-1}$ (Fig. 7b).[16] To improve the quality of white light based on lead-free double perovskites, Chen *et al.* doped $Tb^{3+}$ ions into the $Cs_2Na_{0.4}Ag_{0.6}In_{0.97}Bi_{0.03}Cl_6$ double perovskite (TDP) thin film *via* a solution method and the $Tb^{3+}$ dopants were proven to enhance the restructuring of STEs in the TDP. In addition, TPD shows effective injection and carrier recombination abilities. Therefore, a WLED with TDP/host and green carbon dots (G-CDs) as emission layers was fabricated, and its structure is shown in Fig. 7c. It was found that the WLED exhibited excellent white-light emission performance, including a color coordinate of (0.328, 0.329), a CRI as high as 87.7, a CCT value of 5702 K, an EQE of 0.695%, and a high brightness of 3163 cd $m^{-2}$.[19] In addition, Liu's team reported a one-component warm WLED based on an ultra-wideband $MA_2CuCl_3$ emitter with a visible light range of 400 to 800 nm, and the prepared electroluminescent WLED is shown in Fig. 7d.[102] The valence band position of the hole injection layer (HIL) was reduced by incorporation of 20% 4,4′-bis(carbazol-9-yl) biphenyl (CBP) into PVK (poly(9-

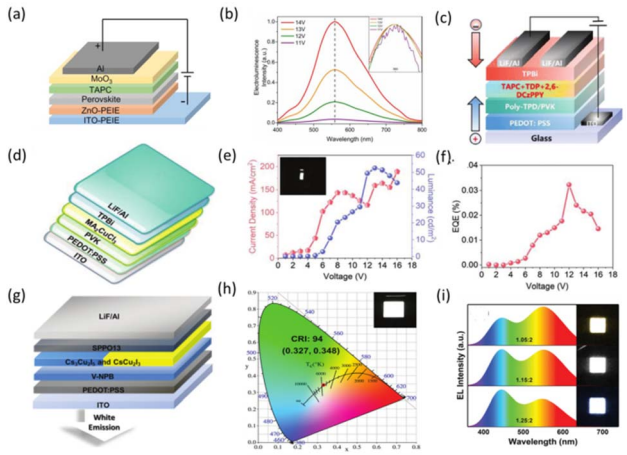

Fig. 7 (a) The electroluminescent device structure.[16] Copyright 2018 Springer Nature Limited. (b) Electroluminescence spectra at an applied voltage of 11 V, 12 V, 13 V and 14 V, respectively. The inset is the normalized spectra.[16] Copyright 2018 Springer Nature. (c) Schematic illustration of white light-emitting diode (WLED) device structure.[19] Copyright 2023 Wiley-VCH. (d) Device structure of $MA_2CuCl_3$ thin-film-based LEDs.[102] Copyright 2022 Wiley-VCH. (e) *I–V–L* characteristics of $MA_2CuCl_3$ LED device.[102] Inset: photograph of the LED driven by a 10 V bias. Copyright 2022 Wiley-VCH. (f) EQE *versus* voltage of these devices.[102] Copyright 2022 Wiley-VCH. (g) Schematic structure of WLEDs.[103] Copyright 2020 Royal Society of Chemistry. (h) CIE chromaticity diagram (inset: photograph of the white device).[103] Copyright 2020 Royal Society of Chemistry. (i) EL spectra of the devices fabricated with different CsI/CuI molar ratios. The insets of (i) show a series of white-light photographs of the devices from cold-white light to warm-white light.[104] Copyright 2020 Wiley-VCH.

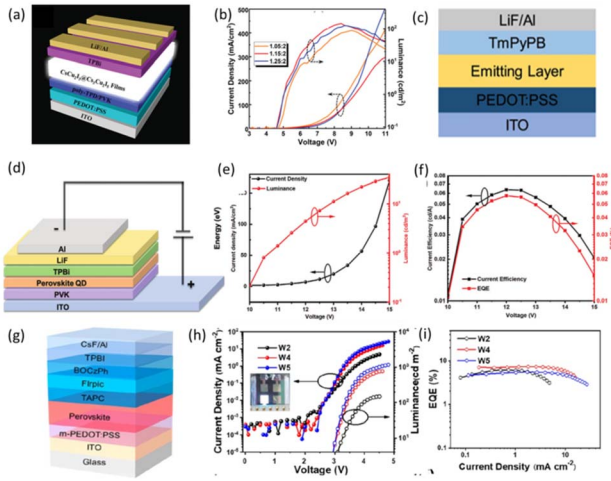

Fig. 8 (a) Schematic structure of the electrically driven WLEDs based on $CsCu_2I_3$@$Cs_3Cu_2I_5$ composite films.[104] Copyright 2020 Wiley-VCH. (b) Current density–voltage–luminance curves of WLEDs with different CsI/CuI molar ratios.[104] Copyright 2020 Wiley-VCH. (c) Schematic diagram of the WLED structure.[110] Copyright 2021 Springer Nature. (d) Structure diagram of $Cs_2AgIn_{0.9}Bi_{0.1}Cl_6$ QDs-based electroluminescence WLEDs.[111] (e) Dependence of the current density and luminance on the driving voltage.[111] (f) Dependence of the current efficiency and EQE on the driving voltage.[111] Copyright 2021 Wiley-VCH. (g) Schematic diagram of the device structure of the perovskite/organic hybrid white LEDs.[112] (h) *J–V–L* (inset: photograph of working device W4) and (i) EQE–*J* characteristics of devices W2, W4, and W5.[112] Copyright 2022 American Chemical Society.

vinylcarbazole)), resulting in significant white-light emission at a bias voltage of 7 to 13 V. Fig. 7e gives the current–volt–brightness (*I–V–L*) characteristics of the $MA_2CuCl_3$ LED, and the inset shows a photograph of the LED driven at a 10 V bias. The required on-voltage of the LED is about 6 V, the maximum brightness is 54 cd $m^{-2}$, and the maximum EQE is 0.035% (Fig. 7f).

However, the CRI values of reported single-component white emitters are generally small and not suitable for efficient white-lighting performance.[51] Therefore, multi-component Cu-based perovskite WLEDs with STE characteristics have attracted the interest of researchers. Zhu *et al.* easily realized a controllable and reversible phase transition between $Cs_3Cu_2I_5$ and $CsCu_2I_3$ *via* solvent treatment, and achieved white-light emission. The electroluminescent device structure and CIE chromaticity diagram are shown in Fig. 7g and h, respectively. The on-voltage is only 2.9 V at 1 cd $m^{-2}$, and the maximum current efficiency is 0.11 cd $A^{-1}$. The EQE is 0.053%.[103] At the same time, Shan *et al.* prepared a $CsCu_2I_3$@$CsCu_2I_5$ composite using different ratios of CsI and CuI, and the composite showed ideal white-light emission with cold and warm white-light tuning as shown in Fig. 7i. They produced electroluminescent WLEDs with a multi-layer structure of ITO/PEDOT:PSS/poly-TPD/PVK/$CsCu_2I_3$@$Cs_3Cu_2I_5$/TPBi/LiF/Al, and the device schematic diagram is shown in Fig. 8a. They experimented with WLEDs by creating three devices with a CsI/CuI molar ratio of 1.05 : 2, 1.15 : 2, and 1.25 : 2, respectively. As shown in Fig. 8b, the current density–voltage–brightness curves of the three devices showed that, above the initial voltage, the current density and brightness of the devices increased sharply, yielding a maximum luminance of 145 cd $m^{-2}$ at 8.4 V for the WLED with the CsI/CuI molar ratio of 1.15 : 2 and an EQE value of 0.15%. It is worth mentioning that the CRI value obtained was as high as 91.6.[104] However, the electronic properties of cesium copper iodides are disadvantageous for LEDs because of the large effective mass of the carriers,[113] and poor charge transport due to the large band gap.[114] They found that the photoelectronic properties of cesium copper iodides could be significantly enhanced by simply chemically adsorbing ether groups to the metal-halide surfaces as electron donors. Based on this strategy, Wang *et al.* fabricated WLEDs based on a prepared 0D $Cs_3Cu_2I_5$ and 1D $CsCu_2I_3$ mixture, as shown in Fig. 8c.[110] WLEDs exhibit broadband EL spectra with a CIE coordinate of (0.44, 0.53), and display luminance up to 1570 cd $m^{-2}$ at a low voltage of 5.4 V. Perovskite quantum dots have been widely used in WLEDs because of their high quantum yields, adjustable band gap and simple preparation.[111] In addition to white-light emitting perovskites as the emission layer of the device, perovskites that emit non-white light such as blue, red or green light can also be used as light-emitting layers. Zhang *et al.* prepared an electroluminescent WLED based on lead-free double perovskite $Cs_2AgIn_{0.9}Bi_{0.1}Cl_6$ quantum dots with red and purple dual-color emission. They chose PVK as the hole transport layer, and purple radiation of PVK effectively compensated for purple radiation of quantum dots, and

luminous performance remained unchanged. The device structure is shown in Fig. 8d. The current density–voltage ($J$–$V$) and light–emitting voltage ($L$–$V$) curves of QD WLEDs are shown in Fig. 8e. The on-voltage (at 1 cd $m^{-2}$) is 10 V, and the brightness value is 34.7 cd $m^{-2}$ (15 V). As shown in Fig. 8f, the maximum current efficiency and EQE are 0.058 cd $A^{-1}$ and 0.064%, respectively. Finally, they chose triphenylphosphine oxide (TPPO) to fill tiny gaps among the quantum dots, and increased the maximum brightness and EQE to 158 cd $m^{-2}$ and 0.08%, respectively.[111] Su *et al.* combined a successively stacked pure-red-light-emitting lead-free perovskite with a sky-blue-light-emitting organic p–i–n heterojunction to achieve coordinated white-light emission. The device structure is shown in Fig. 8g, where an ultra-thin undoped organic phosphorescent intermediate layer (FIrpic) is sandwiched between a p-type hole transport layer (p-HTL) (TAPC) and an n-type electron transport layer (n-ETL) (BOCzPh) to form a sky-blue-light glowing organic p–i–n heterojunction unit. They investigated different thicknesses of perovskite layers at 50, 40 and 30 nm in devices designated as W2, W4 and W5, respectively. It can be seen from Fig. 8h that the brightness gradually increases as the thickness of the perovskite layer decreases. As shown in Fig. 8i, although W5's maximum brightness climbed to 1162 cd $m^{-2}$, its EQE peak decreased to 5.54%. By adjusting the thickness, the peak EQE of the final device is 7.35%, the brightness is 746 cd $m^{-2}$, the CIE coordinate is (0.424, 0.363), and the CCT value is 2868 K.[112] Similarly, other perovskites with high luminous efficiency and stable red-light emission can also be applied; for example, the red LED made by Lee's team can also be used to prepare white LEDs with this strategy.[115] It is noteworthy that lead-free perovskites with other emitters enable electroluminescent emission using this strategy. Wang *et al.* utilized the efficient blue-light emission of $Cs_3Cu_2I_5$ to realize white-light emission.[79]

However, up to now, electroluminescent WLEDs based on lead-free environment-friendly metal halides are still at the initial stage, and the performance of the devices obtained is far less than that of WLEDs based on lead-based perovskites.[117–119] Therefore, it is also necessary to improve the efficiencies of the electroluminescent WLEDs based on LFMHP materials to meet the requirements of various applications.

### Photoluminescent (PL) WLEDs based on LFMHPs

It has been reported that a simple mixture of yellow and blue light facilitates white-light emission. In 2017, Ma *et al.* reported a series of lead-free organic-methane halides $(C_4N_2H_{14}X)_4SnX_6$ (X = Br, I) and $(C_9NH_{20})_2SbX_5$ (X = Cl) with 0D structures. The yellow-light-emitting $(C_4N_2H_{14}Br)_4SnBr_6$ is mixed with commercial blue-light-emitting phosphors ($BaMgAl_{10}O_{17}$:$Eu^{2+}$) in different ratios. The emission spectra for the mixtures with different ratios under UV irradiation are shown in Fig. 9a. The variety of CCT values implies that the white light can be adjusted from "cold" to "warm" (Fig. 9b). When the ratio of two emitters is 1 : 1, the CIE coordinates of the obtained white-light emission are (0.35, 0.39), and its CCT and CRI values are 4946 K and 70, respectively. Under different operating currents, the color stability of this white-light LED is very good, as shown in Fig. 9c.[116] However, the low PLQYs of intrinsic LFMHPs still hinder their practical application in optoelectronic devices. Xia *et al.* doped $Sb^{3+}$ ions into 0D-structure $Cs_2InCl_5\cdot H_2O$ single crystals to achieve broadband yellow-light emission with a PLQY of up to 95.5%, as shown in Fig. 9d. They then prepared WLEDs with $Cs_2InCl_5\cdot H_2O$:$Sb^{3+}$ and the blue-light-emitting $BaMgAl_{10}O_{17}$:$Eu^{2+}$ phosphor in epoxy resin. Fig. 9e shows the PL spectrum of the WLED device at 20 mA current. As shown in Fig. 9f, the CIE coordinate of the fabricated WLED is (0.3576, 0.3547), corresponding to a CRI of 86, and a CCT value of 4556 K.[34] However, due to the lack of red and orange emissions, WLEDs with yellow phosphors combined with blue chips usually emit cold white light. Therefore, Li *et al.* doped $Mn^{2+}$ into yellow-light-emitting $(C_8H_{17}NH_2)_2SnBr_4$ to enable orange-red-light emission, and combined prepared phosphors with commercial blue phosphors to manufacture WLEDs. As shown in Fig. 9g, h and i, the color coordinates of the WLEDs based on doped metal halides are located in the warmer color region, and they exhibited an increased CRI of 88.12 and a CCT of 3542 K.[57]

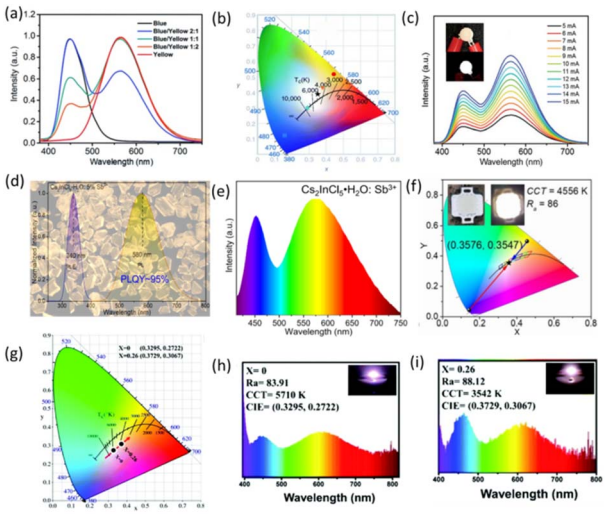


Fig. 9 (a) Emission spectra of UV-pumped LEDs with different blending ratios of blue and yellow phosphors.[116] Copyright 2017 Royal Society of Chemistry. (b) CIE coordinates and CCTs for UV-pumped LEDs plotted on the CIE 1931 chromaticity chart.[116] Copyright 2017 Royal Society of Chemistry. (c) Emission spectra of a white LED at different driving currents; insets show the operating device.[116] Copyright 2017 Royal Society of Chemistry. (d) PLE (with monitoring wavelength at 580 nm) and PL (with excitation wavelength at 340 nm) spectra of $Cs_2InCl_5\cdot H_2O$:5% $Sb^{3+}$.[34] Copyright 2020 American Chemical Society. (e) PL spectra of the UV-pumped WLED based on $Cs_2InCl_5\cdot H_2O$:$Sb^{3+}$ at 20 mA drive current.[34] Copyright 2020 American Chemical Society. (f) CIE coordinates and CCTs for the UV pumped LEDs plotted on the CIE1931 chromaticity chart.[34] Copyright 2020 American Chemical Society. (g) Color coordinates and (h) image and emission spectrum of a white LED fabricated by $(C_8H_{17}NH_2)_2$-$Sn_{1-x}Mn_xBr_4$ ($x = 0$) phosphors combined with BAM commercial blue powder driven by a UV chip ($\lambda_{em}$ = 365 nm).[57] Copyright 2022 Royal Society of Chemistry. (i) Image and emission spectrum of a white LED fabricated by $(C_8H_{17}NH_2)_2Sn_{1-x}Mn_xBr_4$ ($x = 0.26$) phosphors combined with BAM commercial blue powder driven by a UV chip ($\lambda_{em}$ = 365 nm).[57] Copyright 2022 Royal Society of Chemistry.

Additionally, luminescent WLEDs can be fabricated with the assistance of mixed red, green and blue emitters. High-efficiency blue-light-emitting lead-free perovskite phosphors are firstly used to make WLEDs. Jing *et al.* synthesized $[H_2AMPd]ZnBr_4 \cdot H_2O$ with strong blue-light emission and mixed it with commercial (Sr, Ca)$AlSiN_3$:Eu as a red phosphor to prepare WLEDs, which displayed bright white light, as shown in Fig. 10a and b, with a CCT of 5273 K, CIE chrominance coordinates of (0.33, 0.33), and a CRI of 94.5.[120] Hu *et al.* doped $Bi^{3+}$ into $Cs_2ZrCl_6$ to make it emit blue light and they found that $Cs_2ZrCl_6$:$Bi^{3+}$ has a strong water-resistant core–shell structure and durable luminescence characteristics. After two hours of immersion in water, the luminescence intensity even increased to 115.94% of the initial level. Mixed with green and red commercial phosphors on UV chips, as shown in Fig. 10c, the WLEDs demonstrated CIE coordinates of (0.37, 0.35) and a CCT of 4179 K.[121]

In addition, lead-free perovskites with green-light luminescence have also been developed. Zang *et al.* mixed green $(TBA)_2MnBr_4$ single crystals with commercial red $CaAlSiN_3$:$Eu^{2+}$ phosphors (630 nm) and blue InGaN chips (450 nm) to fabricate WLEDs. As shown in Fig. 10d, their CCT and CRI values were 5864 K and 80, respectively.[84] In order to further enhance the green luminescence, Chen *et al.* doped $Cu^+$ into $Cs_2MnCl_4$, whose CIE coordinates are displayed in Fig. 10e, and prepared WLEDs with a coating of blue BAM:$Eu^{2+}$ and red CASN:$Eu^{2+}$ phosphors. As shown in Fig. 10f, the prepared WLEDs have a high CRI of 93 and a low CCT of 4080 K.[122] More interestingly, Jiang *et al.* doped $Sb^{3+}$ ions into the In-based lead-free halides of $Cs_2InCl_5(H_2O)$:$Sb^{3+}$: yellow, $Cs_3InCl_6$:$Sb^{3+}$: green, and $Cs_2NaInCl_6$:$Sb^{3+}$: blue. Three-color phosphors were mixed to fabricate WLEDs, as shown in Fig. 10g. It was seen from a comparison of Fig. 10h and i that the WLEDs with $Cs_3InCl_6$:$Sb^{3+}$ have a higher CRI of 95.4.[123] This has greatly promoted the development of lead-free halide emitters, providing new possibilities for manufacture of high-color rendering WLEDs.

Furthermore, the mergence of WLEDs based on single-component LFMHPs can solve some issues of multi-component metal-halide WLEDs.[127–133] In 2021, He Shao *et al.* prepared lead-free 0D $K_3SbCl_6$ perovskites with a blue-light emission center at 440 nm and a PLQY of 22.3%.[74] By introducing $Mn^{2+}$ ions into 0D $K_3SbCl_6$ perovskites, the white light was realized by controlling the doping concentration of $Mn^{2+}$ ions. As shown in Fig. 11a, the energy transition from the $^4T_1$–$^6A_1$ levels to the $Mn^{2+}$ states is proved, which is due to the deformation of the lattices with the increase of $Mn^{2+}$ ion concentration.[134] In $Mn^{2+}$-$K_3SbCl_6$ NCs, STEs in the perovskites

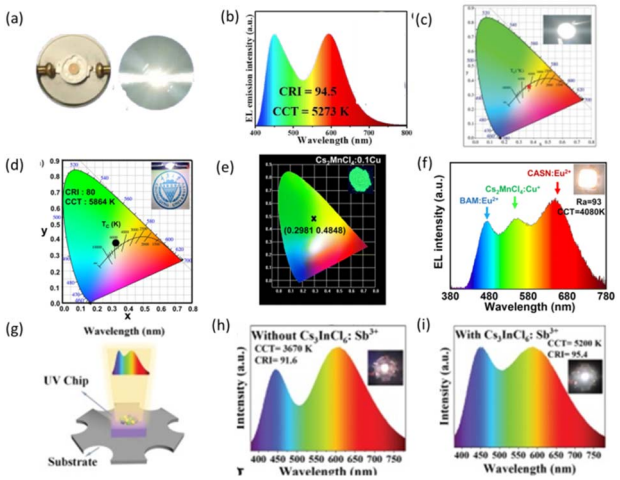


Fig. 10 (a) Photograph of obtained white LED.[120] Copyright 2023 Elsevier Ltd. (b) EL emission spectrum under 120 mA drive current.[120] Copyright 2023 Elsevier Ltd. (c) CIE color coordinates of the WLED device is denoted by the red star. The inset is a photo of the WLED device in operation.[121] Copyright 2020 WILEY-VCH. (d) A CIE chromaticity diagram of the WLEDs, with the inset showing a photograph of a WLED. Copyright Elsevier B.V. (e) Chromaticity coordinates (1931) of $Cs_2MnCl_4$:0.1$Cu^+$.[122] (f) Electroluminescence spectrum of the WLED fabricated using a 310 nm chip and $BaMgAl_{10}O_{17}$:$Eu^{2+}$, $CaAlSiN_3$:$Eu^{2+}$ and $Cs_2MnCl_4$:0.1$Cu^+$ phosphors (the inset shows the photograph of the as-packaged LED lighting).[122] Copyright 2023 Royal Society of Chemistry. (g) Schematic configuration of the WLED device fabricated from a 317 nm chip encapsulated with a mixture of phosphors consisting of $Cs_2NaInCl_6$:$Sb^{3+}$, $Cs_3InCl_6$:$Sb^{3+}$, and $Cs_2InCl_5(H_2O)$:$Sb^{3+}$.[123] (h) Electroluminescence spectrum of a WLED based on $Cs_2NaInCl_6$:-$Sb^{3+}$ and $Cs_2InCl_5(H_2O)$:$Sb^{3+}$ pumped by 317 nm chip.[123] (i) EL spectrum of a WLED based on $Cs_2NaInCl_6$:$Sb^{3+}$, $Cs_2InCl_5(H_2O)$:$Sb^{3+}$, and $Cs_3InCl_6$:$Sb^{3+}$ pumped by a 317 nm chip. The inset shows the corresponding EL photograph of the WLEDs.[123] Copyright 2023 Wiley-VCH GmbH.

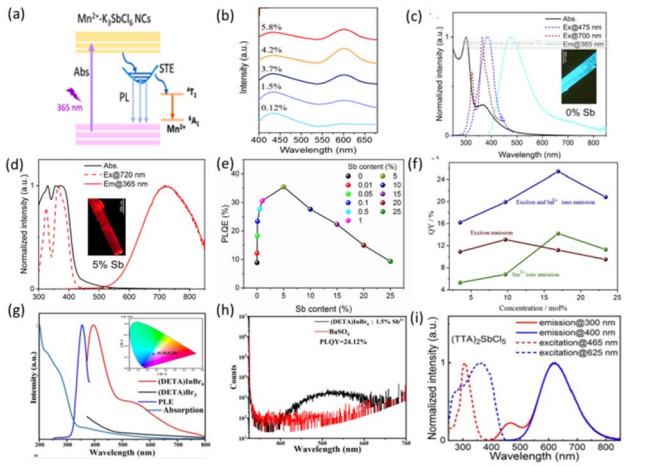


Fig. 11 (a) The proposed PL mechanism for the $Mn^{2+}$-$K_3SbCl_6$ NCs.[74] Copyright 2020 Elsevier B.V. (b) PL emission spectra for $Mn^{2+}$-$K_3SbCl_6$ NCs with different doping concentrations under excitation of 365 nm.[74] Copyright 2020 Elsevier B.V. (c) Absorption, PLE, and PL spectra of $(C_8NH_{12})_6InBr_9 \cdot H_2O$.[124] Copyright 2020 American Chemical Society. (d) Absorption, PLE, and PL spectra of $(C_8NH_{12})_6InBr_9 \cdot H_2O$:5% Sb sample.[124] Copyright 2020 American Chemical Society. (e) PLQE variation *vs.* different Sb doping contents upon 365 nm excitation.[124] Copyright 2020 American Chemical Society. (f) PLQYs of exciton emission *versus* $Sm^{3+}$ doping concentrations in $Cs_3Bi_2Br_9$ PQDs.[61] Copyright 2020 Chinese Society of Rare Earths. (g) PLE and PL spectra of (DETA)$InBr_6$ ($\lambda_{ex}$ = 353 nm) and (DETA)$Br_3$.[125] Copyright 2023 American Chemical Society. (h) PLQYs of (DETA)$InBr_6$:1.5%$Sb^{3+}$.[125] Copyright 2023 American Chemical Society. (i) PLE and PL spectra of $(TTA)_2SbCl_5$.[126] Copyright 2019 American Chemical Society.

together with the intrinsic transition of the dopant $Mn^{2+}$ ions results in white-light emission. When the doping concentration of $Mn^{2+}$ ions is 3.7%, 4.2% and 5.8%, the white-light luminescence CIE coordinates of the $Mn^{2+}$-$K_3SbCl_6$ NCs were (0.29, 0.29), (0.34, 0.31) and (0.33, 0.30), respectively. In addition, as shown in Fig. 11b, they found that upon further increasing the doping concentration of $Mn^{2+}$ ions, the relative emission intensity of the STEs for the intrinsic transition of $Mn^{2+}$ ions continuously decreased due to the concentration quenching of dopants.[74] The intrinsic lead-free perovskites were found to exhibit extra spectral ranges induced by incorporation of dopants, and single-component white-light emission can also be realized. Xie *et al.* synthesized $(C_8NH_{12})_6InBr_9 \cdot H_2O$, which showed dual-band emission including strong cyan-light emission and a weak red-light emission tail (Fig. 11c).[124] The doping with $Sb^{3+}$ ions greatly enhanced the low-energy ultra-broadband red-light emission tail, optimized the band gap structure, and promoted red-light STE emission (Fig. 11d), resulting in single-component warm white-light emission with a CIE coordinates of (0.400, 0.361), a CCT of 3347 K, and a CRI of 84 at the Sb concentration of 0.1%.[48] Although a 35% PLQY was obtained when the $Sb^{3+}$ concentration was 5% (Fig. 11e), it cannot emit white light efficiently, indicating that the doping concentration may affect the efficiency of white-light emission. Pan *et al.* doped $Sm^{3+}$ ions into 2D $CsBi_2Br_9$ QDs, which not only enhanced the PLQY from 10.9% to 20.8% (Fig. 11f), but also led to emission of tunable warm white light. The optimized white-light emission possesses CIE coordinates of (0.296, 0.289) and a CCT of 8967 K, as well as better water resistance stability.[61] Wang *et al.* grew 0D white-light-emitting $(C_4H_{16}N_3)InBr_6$ ($C_4H_{13}N_3$(DETA) = diethylenetriamine) LFMHPs through a simple mechanochemical method. The blue-light emission band at 400 nm and the yellow-light emission band at 550 nm are coupled together to produce cold-white-light emission with a PLQY of 1.4%. This phenomenon was caused by the radiative recombination of free excitons and STEs. The CCT and CRI of (DETA)$InBr_6$ are 18 059 K and 91, respectively. Its CIE coordinates are (0.26, 0.26), corresponding to cold-white-light emission (Fig. 11g).[125] In order to achieve highly tunable emission, they doped with $Sb^{3+}$ ions to regulate the photoluminescence. After $Sb^{3+}$ doping, the band-edge absorption was significantly enhanced in the range of 350–430 nm. Moreover, the doping amount of $Sb^{3+}$ had a great influence on the PLQYs, and a maximum PLQY of 24.12% was achieved in (DETA)$InBr_6$:1.5% $Sb^{3+}$ (Fig. 11h). It can be seen that with the increase of $Sb^{3+}$ concentration, the increase of luminescent centers as the energy receptors are transferred from the exciton band led to an enhancement of photoluminescence intensity. Li *et al.*[97] reported 0D $(TTA)_2SbCl_5$ (TTA = tetraethyl ammonium) with dual-band emission under high-energy photon excitation (Fig. 11i and 12a). It can be seen that under 300 nm excitation, dual-band emission and an additional blue-light emission band in $(TTA)_2SbCl_5$ enabled single-component white-light emission with a PLQY of 68%, which was much higher than that of other low-dimensional hybrid LFMHPs.[97] WLEDs based on $(TTA)_2SbCl_5$ exhibited a CCT of 2360 K and a CRI of 84. In addition, their excellent water resistance and thermal stability was

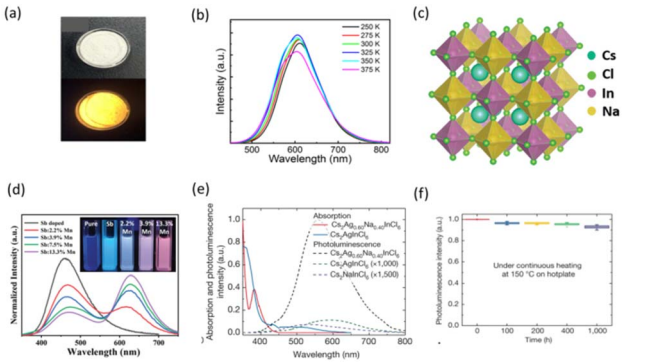


Fig. 12 (a) Photographs of $(TTA)_2SbCl_5$ powder under ambient light (top) and 365 nm UV light (bottom).[126] Copyright 2019 American Chemical Society. (b) The PL spectra of $(TTA)_2SbCl_5$ in the range of 250–375 K.[126] Copyright 2019 American Chemical Society. (c) Crystal structure of $Cs_2NaInCl_6$.[135] (d) Normalized PL spectra of $Cs_2NaInCl_6$ NCs with different doping ratios.[135] (e) Optical absorption (solid lines) and PL (dashed lines) spectra of intrinsic $Cs_2AgInCl_6$ and $Cs_2Ag_{0.60}Na_{0.40}InCl_6$.[16] Copyright 2018 Springer Nature. (f) Photoluminescence stability of $Cs_2Ag_{0.60}Na_{0.40}InCl_6$ against continuous heating at 150 °C on a hotplate, measured after cooling to room temperature.[16] Copyright 2018 Springer Nature.

proved, as shown in Fig. 12b.[126] Double perovskites with broadband white-light emission, high absorption coefficients and fast carrier recombination rates are also of interest to researchers.[136] $Cs_2NaInCl_6$ is a representative cubic double perovskite, which is similar to classic lead halide perovskites, as shown in Fig. 12c. However, due to a forbidden transition in $Cs_2NaInCl_6$, its PLQY is very low. To enhance its optoelectronic properties, Liu *et al.* synthesized millimeter-scale $Cs_2NaInCl_6$ single crystals and co-doped Sb–Mn into them. The co-doped $Cs_2NaInCl_6$ was found to emit warm white light with an enhanced PLQY of 84%, as shown in Fig. 12d.[135] However, blue light with a wavelength below 450 nm is harmful to human bodies and is not suitable for long-term indoor lighting. To solve this problem, Chen *et al.* doped $Sb^{3+}$ ions into $Cs_2NaInCl_{6-x}Br_x$ double perovskites and optimized the halogen ratios. With the increase of Br/Cl ratios, the emission spectra continuously red-shifted from 445 nm (blue light) to 480 nm (cyan light), indicating that they could be employed in WLEDs.[137]

Furthermore, Tang *et al.* prepared $Cs_2(Ag_{0.60}Na_{0.40})InCl_6$ by alloying $Na^+$ ions into $Cs_2AgInCl_6$, and then observed white-light emission by doping with 0.04% Bi ions. After Na alloying, an obvious exciton absorption peak appeared near 365 nm. Fig. 12e shows that the alloyed perovskites exhibited 1000 times higher emission intensity than intrinsic $Cs_2AgInCl_6$, and the highest PLQY of (86 ± 5) % was obtained when the content of Na was about 40%. The powders were directly coated onto commercial UV-LEDs to fabricate WLEDs, which showed CIE coordinates of (0.396, 0.448) and a CCT of 4054 K. When the WLEDs were operated in air for more than 1000 hours at 5000 cd $m^{-2}$, their luminous performance hardly changed, as shown in Fig. 12f, showing their good operating stability.[16] For a PL WLED, stability is crucial, and Table 1 summarizes stability

Table 1 Statistics from the literature on the stability of WLED devices[a]

| Materials | Color | CIE ($x$, $y$) | CCT (K) | CRI | WLED stability | | | Ref. |
|---|---|---|---|---|---|---|---|---|
| | | | | | Light | Air | Water | |
| $(C_4N_2H_{14}Br)_4SnBr_6$ | Yellow | (0.35, 0.39) | 4946 | 70 | — | $T_{98}$ = 6 h | — | 116 |
| $[Na(DMSO)_2]_3SbBr_6$ | Yellow | (0.36, 0.28) | 3603 | 85 | $T_{98}$ = 120 h@440 nm | $T_{57}$ = 130 h | — | 71 |
| $OTA_{2+x}SnI_{4+x}$ | Yellow | (0.45, 0.38) | 3300 | 92 | $T_{98}$ = 25 min@380 nm | — | — | 63 |
| $CsMnBr_3$ | Red | (0.33, 0.36) | 5342 | 94 | — | — | $T_{95}$ = 90 days | 138 |
| $[H_2AMPd]ZnBr_4 \cdot H_2O$ | Blue | (0.33, 0.33) | 5273 | 94.5 | — | $T_{99}$ = 8 h | — | 120 |
| $Cs_2ZrCl_6$:$Bi^{3+}$ | Blue | (0.37, 0.35) | 4486 | 81.9 | $T_{99}$ = 24 h@350 nm | — | $T_{99}$ = 2 h | 121 |
| $[DAPEDA]InCl_6 \cdot Cl \cdot H_2O$:$Sb^{3+}$ | Green | (0.33, 0.34) | 5669 | 93.2 | $T_{90}$ = 240 min@450 nm | — | — | 92 |
| $[DPA]_3InCl_6$:$Sb^{3+}$ | Green | (0.34, 0.35) | 5864 | 80 | — | $T_{50}$ = 240 h | — | 84 |
| $Cs_2MnCl_4$:$Eu^{2+}$ | White | (0.33, 0.27) | — | 90 | — | $T_{90}$ = 20 h | — | 21 |
| $K_3SbCl_6$:$Mn^{2+}$ | White | (0.29, 0.28) | 8173 | >80 | $T_{50}$ = 12 h@365 nm | — | — | 74 |
| $K_3SbCl_6$:$Mn^{2+}$ | White | (0.32, 0.30) | 5068 | >80 | — | — | — | 74 |
| $K_3SbCl_6$:$Mn^{2+}$ | White | (0.35, 0.30) | 4779 | >80 | — | — | — | 74 |
| $Cs_3Cu_2Cl_5$@$CsCu_2Cl_3$ | White | (0.34, 0.34) | 5285 | 94 | — | $T_{64}$ = 60 h | — | 77 |
| $Cs_3Cu_2Cl_5$@$CsCu_2Cl_3$ | White | (0.36, 0.37) | 4516 | 89 | — | $T_{98}$ = 120 h | — | 139 |
| $Cs_2Ag_{0.6}Na_{0.4}InCl_6$:30% Bi | White | — | 6585 | — | — | $T_{95}$ = 10 h | $T_{90}$ = 10 h | 140 |
| $Cs_2Ag_{0.6}Na_{0.4}InCl_6$:0.05% Bi | White | (0.40, 0.45) | 4054 | — | — | $T_{92}$ = 1000 h | — | 16 |
| $Cs_2Ag_{0.4}Na_{0.6}In_{0.9}Bi_{0.1}Cl$:$Ho^{3+}$/$Yb^{3+}$ | White | (0.34, 0.36) | — | — | — | $T_{89}$ = 5 h | — | 141 |

[a] $T_n$: required time for luminescence intensity to decrease to $n$% of the initial values in WLEDs.

details of reported WLEDs against light, air and water, implying the effect of emitters on the stability of WLEDs.

## Challenges and perspectives

In recent years, LFMHPs have been widely utilized in solar cells, light-emitting diodes, lasers and photodetectors due to their excellent optoelectronic characteristics and properties. Importantly, the attractive luminescence performance of LFMHPs enables them to be used as emitting sources of WLEDs, facilitating potential applications in display and lighting. Therefore, researchers have paid more attention to the structures and emission mechanisms of LFMHPs, as well as optimization of WLED performance. In this work, we have reviewed structures of LFMHPs with different dimensions and common preparation methods. We focused on the principles of photoluminescent and electroluminescent WLEDs based on LFMHPs, and summarized and analyzed their performance. However, WLEDs based on LFMHPs face several problems and challenges, which may impede their further enhancement of performance and limit their potential applications. The current challenges and perspectives of WLEDs based on LFMHPs are summarized and highlighted as follows:

Light-emitting devices based on LFMHPs have been the subject of numerous studies and improvements in the performance optimization of environmentally-friendly WLEDs has been shown. LFMHPs possess high fluorescence efficiencies, narrow luminescence peaks, and adjustable emission spectra covering the entire visible range, but there are still challenges with regard to their high-efficiency photoluminescence and electroluminescence operation. For photoexcited WLEDs, their luminous efficiencies often depend on the output power of the excitation chips and the PLQYs of the LFMHPs. However, the luminous efficiencies of the photoluminescent WLEDs are far below those of commercial sources. In addition, LFMHPs exhibit strong absorption in the ultraviolet and deep ultraviolet regions, however, short-wavelength chips (below 365 nm) used as a common excitation source for WLEDs have lower output power than blue chips, resulting in a large loss of efficiency. Therefore, enhancement of PLQYs in LFMHPs under UV excitation enables the efficiencies of WLEDs based on LFMHPs to be increased. By optimizing and minimizing the lattice deformation energy and self-trapping energy of LFMHPs, the structure of the LFMHPs can be tuned and their defects suppressed, thereby improving their PLQYs. According to previous reports, ion doping is considered to be an effective strategy to regulate the band structures of LFMHPs and improve their luminescence performance. In addition, compared with multi-component WLEDs, fabrication of single-component WLEDs simplifies the preparation processes and can decrease the deterioration of luminous efficiencies caused by the mismatch of LFMHPs.

Apart from high luminous efficiencies, excellent stabilities of WLEDs are also required. It has been reported that the operating lifetime of an LFMHP-based photoluminescent WLED is below 1000 hours, which cannot meet the requirements of >10 000 hours for commercial lighting applications. During long-term operation of a WLED, heat is generated, and with the increase of temperature, this may lead to disintegration of the LFMHPs, which deteriorates the performance of the WLED. In addition, some LFMHPs are found to decompose when exposed to water, so it is very important to explore and optimize LFMHPs with excellent heat and water resistance. Therefore, further research on the degradation mechanism of LFMHPs is needed, and various modification and encapsulation technologies should continue to be explored. Researchers have proposed doping and coating strategies to protect LFMHPs from heat and water, thereby improving the working performance of WLEDs.

Additionally, good surface ligands can be introduced onto LFMHP NCs to reduce their sensitivity to heat and water. In summary, research of WLEDs based on LFMHPs has made remarkable progress in materials development, device design and performance improvement, but there are still many challenges, such as improving electroluminescence efficiencies and stabilities, as well as exploring materials synthesis and luminescence mechanisms. These studies are important for promoting the development of next-generation display and lighting technologies.

## Data availability

No primary research results, software or code have been included and no new data were generated or analysed as part of this review.

## Author contributions

Z. Z. and S. Z. directed this review. R. T. performed the literature search and organized the content. All authors collaborated on the data analysis and participated in writing the paper.

## Conflicts of interest

There are no conflicts to declare.

## Acknowledgements

This work is funded by National Natural Science Foundation of China (No. 11974063); Young Elite Scientists Sponsorship Program by CAST (No. 2022QNR001).

## Notes and references

1 E. F. Schubert and J. K. Kim, *Science*, 2005, **308**, 1274–1278.
2 H. Amano, M. Kito, K. Hiramatsu and I. Akasaki, *Jpn. J. Appl. Phys.*, 1989, **28**, L2112–L2114.
3 S. Nakamura, T. Mukai and M. Senoh, *Appl. Phys. Lett.*, 1994, **64**, 1687–1689.
4 B. M. Benin, D. N. Dirin, V. Morad, M. Worle, S. Yakunin, G. Raino, O. Nazarenko, M. Fischer, I. Infante and M. V. Kovalenko, *Angew. Chem., Int. Ed.*, 2018, **57**, 11329–11333.
5 S. Zhao, J. Zhao, S. M. H. Qaid, D. Liang, K. An, W. Cai, Q. Qian and Z. Zang, *Appl. Phys. Rev.*, 2024, **11**, 011408.
6 S. Zhao, S. Jiang, W. Cai, R. Li, Q. Mo, B. Wang and Z. Zang, *Cell Rep. Phys. Sci.*, 2021, **2**, 100585.
7 D. Liang, Z. Sun, S. Lu, J. Zhao, Y. Zhou, K. An and Z. Zang, *Inorg. Chem.*, 2023, **62**, 7296–7303.
8 S. Wang, X. Han, T. Kou, Y. Zhou, Y. Liang, Z. Wu, J. Huang, T. Chang, C. Peng, Q. Wei and B. Zou, *J. Mater. Chem. C*, 2021, **9**, 4895–4902.
9 R. Fan, S. Fang, C. Liang, Z. Liang and H. Zhong, *Photonics Res.*, 2021, **9**, 694–700.
10 A. Yan, K. Li, Y. Zhou, Y. Ye, X. Zhao and C. Liu, *J. Alloys Compd.*, 2020, **822**, 153528.
11 H. Cho, Y. H. Kim, C. Wolf, H. D. Lee and T. W. Lee, *Adv. Mater.*, 2018, **30**, e1704587.
12 C. Zhao, Y. Yu, J. Dai, Y. Zu and Z. Wu, *Chin. Sci. Bull.*, 2021, **66**, 2139–2150.
13 F. Liu, C. Ding, Y. Zhang, T. Kamisaka, Q. Zhao, J. M. Luther, T. Toyoda, S. Hayase, T. Minemoto, K. Yoshino, B. Zhang, S. Dai, J. Jiang, S. Tao and Q. Shen, *Chem. Mater.*, 2019, **31**, 798–807.
14 X. Wang, X. Hong, B. Yang, Y. Chen and J. Zou, *ECS J. Solid State Sci. Technol.*, 2021, **10**, 065011.
15 X. Zhang, Z. Jin, J. Zhang, D. Bai, H. Bian, K. Wang, J. Sun, Q. Wang and S. F. Liu, *ACS Appl. Mater. Interfaces*, 2018, **10**, 7145–7154.
16 J. Luo, X. Wang, S. Li, J. Liu, Y. Guo, G. Niu, L. Yao, Y. Fu, L. Gao, Q. Dong, C. Zhao, M. Leng, F. Ma, W. Liang, L. Wang, S. Jin, J. Han, L. Zhang, J. Etheridge, J. Wang, Y. Yan, E. H. Sargent and J. Tang, *Nature*, 2018, **563**, 541–545.
17 R. Wang, H. Xiang, J. Chen, Y. Li, Y. Zhou, W. C. H. Choy, Z. Fan and H. Zeng, *ACS Energy Lett.*, 2022, **7**, 2173–2188.
18 S. Zhao, W. Cai, H. Wang, Z. Zang and J. Chen, *Small Methods*, 2021, **5**, e2001308.
19 S. Jin, H. Yuan, T. Pang, M. Zhang, J. Li, Y. Zheng, T. Wu, R. Zhang, Z. Wang and D. Chen, *Adv. Mater.*, 2024, **36**, e2308487.
20 Q. Mo, Y. Shi, W. Cai, S. Zhao, Y. Ying and Z. Zang, *J. Phys. D: Appl. Phys.*, 2022, **55**, 333003.
21 J. Hou, J. Wu, Y. Fang, Y. Wei, L. Dong, G. Zhang, Y. Liu, H. Chen and G. Li, *ACS Appl. Mater. Interfaces*, 2024, **16**, 30176–30184.
22 D. Liang, L. Tan, S. Lu, Z. Sun, H. Wang, W. Cai and Z. Zang, *ACS Appl. Mater. Interfaces*, 2023, **15**, 24622–24628.
23 D. Liang, H. Xiao, W. Cai, S. Lu, S. Zhao, Z. Zang and L. Xie, *Adv. Opt. Mater.*, 2023, **11**, 2202997.
24 G. E. Eperon, S. D. Stranks, C. Menelaou, M. B. Johnston, L. M. Herz and H. J. Snaith, *Energy Environ. Sci.*, 2014, **7**, 982–988.
25 Z. K. Tan, R. S. Moghaddam, M. L. Lai, P. Docampo, R. Higler, F. Deschler, M. Price, A. Sadhanala, L. M. Pazos, D. Credgington, F. Hanusch, T. Bein, H. J. Snaith and R. H. Friend, *Nat. Nanotechnol.*, 2014, **9**, 687–692.
26 Y. Hassan, J. H. Park, M. L. Crawford, A. Sadhanala, J. Lee, J. C. Sadighian, E. Mosconi, R. Shivanna, E. Radicchi, M. Jeong, C. Yang, H. Choi, S. H. Park, M. H. Song, F. De Angelis, C. Y. Wong, R. H. Friend, B. R. Lee and H. J. Snaith, *Nature*, 2021, **591**, 72–77.
27 B. Zhao, S. Bai, V. Kim, R. Lamboll, R. Shivanna, F. Auras, J. M. Richter, L. Yang, L. Dai, M. Alsari, X.-J. She, L. Liang, J. Zhang, S. Lilliu, P. Gao, H. J. Snaith, J. Wang, N. C. Greenham, R. H. Friend and D. Di, *Nat. Photonics*, 2018, **12**, 783–789.
28 K. Lin, J. Xing, L. N. Quan, F. P. G. de Arquer, X. Gong, J. Lu, L. Xie, W. Zhao, D. Zhang, C. Yan, W. Li, X. Liu, Y. Lu, J. Kirman, E. H. Sargent, Q. Xiong and Z. Wei, *Nature*, 2018, **562**, 245–248.

29 C. Chen, J. Xiang, Y. Chen, M. Jin, J. Zheng, N. Zhang and C. Guo, *Ceram. Int.*, 2022, **48**, 1851–1856.
30 X. Zhang, H. Wang, S. Wang, Y. Hu, X. Liu, Z. Shi, V. L. Colvin, S. Wang, W. W. Yu and Y. Zhang, *Inorg. Chem.*, 2020, **59**, 533–538.
31 G. Yang, S. Bai, X. Li, H. Liang, C. Li, J. Sun, Y. Wang, J. Huang, G. Pan and Y. Zhu, *ACS Appl. Mater. Interfaces*, 2023, **15**, 24629–24637.
32 J. Mao, D. Venugopal, Y. Zhang, P. Zhu and G. Wang, *Chem. Eng. J.*, 2023, **470**, 144160.
33 X. Hao, H. Liu, W. Ding, F. Zhang, X. Li and S. Wang, *J. Phys. Chem. Lett.*, 2022, **13**, 4688–4694.
34 Y. Jing, Y. Liu, X. Jiang, M. S. Molokeev, Z. Lin and Z. Xia, *Chem. Mater.*, 2020, **32**, 5327–5334.
35 E. Cui, X. Yuan, L. Tang, L. Yang, X. Yang, X. Liao, J. Tang, Y. Zhao, W. Sun, K. Liu, Y. Liu and J. Liu, *Appl. Surf. Sci.*, 2023, **609**, 155472.
36 M. Lyu, J. H. Yun, P. Chen, M. Hao and L. Wang, *Adv. Energy Mater.*, 2017, **7**, 1602512.
37 S. Li, Z. Shi, F. Zhang, L. Wang, Z. Ma, D. Wu, D. Yang, X. Chen, Y. Tian, Y. Zhang, C. Shan and X. Li, *ACS Appl. Mater. Interfaces*, 2020, **12**, 46330–46339.
38 P. Han, C. Luo, S. Yang, Y. Yang, W. Deng and K. Han, *Angew. Chem., Int. Ed.*, 2020, **59**, 12709–12713.
39 H. Peng, B. Zou, Y. Guo, Y. Xiao, R. Zhi, X. Fan, M. Zou and J. Wang, *J. Mater. Chem. C*, 2020, **8**, 6488–6495.
40 I. Borriello, G. Cantele and D. Ninno, *Phys. Rev. B*, 2008, **77**, 235214.
41 T. C. Jellicoe, J. M. Richter, H. F. J. Glass, M. Tabachnyk, R. Brady, S. E. Dutton, A. Rao, R. H. Friend, D. Credgington, N. C. Greenham and M. L. Böhm, *J. Am. Chem. Soc.*, 2016, **138**, 2941–2944.
42 S. E. Creutz, E. N. Crites, M. C. De Siena and D. R. Gamelin, *Nano Lett.*, 2018, **18**, 1118–1123.
43 L. Zhou, Y. F. Xu, B. X. Chen, D. B. Kuang and C. Y. Su, *Small*, 2018, **14**, e1703762.
44 Q. Liao, J. Chen, L. Zhou, T. Wei, L. Zhang, D. Chen, F. Huang, Q. Pang and J. Z. Zhang, *J. Phys. Chem. Lett.*, 2020, **11**, 8392–8398.
45 Z. Li, F. Sun, H. Song, H. Zhou, Y. Zhou, Z. Yuan, P. Guo, G. Zhou, Q. Zhuang and X. Yu, *Dalton Trans.*, 2021, **50**, 9804–9811.
46 M. D. Smith, B. A. Connor and H. I. Karunadasa, *Chem. Rev.*, 2019, **119**, 3104–3139.
47 S. Ma, M. Cai, T. Cheng, X. Ding, X. Shi, A. Alsaedi, T. Hayat, Y. Ding, Z. a. Tan and S. Dai, *Sci. China Mater.*, 2018, **61**, 1257–1277.
48 L. Mao, P. Guo, M. Kepenekian, I. Hadar, C. Katan, J. Even, R. D. Schaller, C. C. Stoumpos and M. G. Kanatzidis, *J. Am. Chem. Soc.*, 2018, **140**, 13078–13088.
49 M. I. Saidaminov, O. F. Mohammed and O. M. Bakr, *ACS Energy Lett.*, 2017, **2**, 889–896.
50 L. Protesescu, S. Yakunin, M. I. Bodnarchuk, F. Krieg, R. Caputo, C. H. Hendon, R. X. Yang, A. Walsh and M. V. Kovalenko, *Nano Lett.*, 2015, **15**, 3692–3696.
51 Y. Wang, F. Zhang, J. Ma, Z. Ma, X. Chen, D. Wu, X. Li, Z. Shi and C. Shan, *EcoMat*, 2022, **4**, e12160.
52 B. Yang, J. Chen, S. Yang, F. Hong, L. Sun, P. Han, T. Pullerits, W. Deng and K. Han, *Angew. Chem., Int. Ed.*, 2018, **57**, 5359–5363.
53 L. Li, H. Shao, X. Wu, W. Chen, J. Zhu, B. Dong, L. Xu, W. Xu, J. Hu, M. Zhou, Y. Ji, H. Song and X. Bai, *Mater. Res. Bull.*, 2022, **147**, 111645.
54 F. Locardi, M. Cirignano, D. Baranov, Z. Dang, M. Prato, F. Drago, M. Ferretti, V. Pinchetti, M. Fanciulli, S. Brovelli, L. De Trizio and L. Manna, *J. Am. Chem. Soc.*, 2018, **140**, 12989–12995.
55 K. G. Lim, H. B. Kim, J. Jeong, H. Kim, J. Y. Kim and T. W. Lee, *Adv. Mater.*, 2014, **26**, 6461–6466.
56 L. Hou, Y. Zhu, J. Zhu and C. Li, *J. Phys. Chem. C*, 2019, **123**, 31279–31285.
57 L. Hou, Y. Zhu, J. Zhu, Y. Gong and C. Li, *J. Mater. Chem. C*, 2020, **8**, 8502–8506.
58 M. Leng, Y. Yang, K. Zeng, Z. Chen, Z. Tan, S. Li, J. Li, B. Xu, D. Li, M. P. Hautzinger, Y. Fu, T. Zhai, L. Xu, G. Niu, S. Jin and J. Tang, *Adv. Funct. Mater.*, 2018, **28**, 1704446.
59 Z. Z. Ma, Z. F. Shi, L. T. Wang, F. Zhang, D. Wu, D. W. Yang, X. Chen, Y. Zhang, C. X. Shan and X. J. Li, *Nanoscale*, 2020, **12**, 3637–3645.
60 N. Ding, D. Zhou, G. Pan, W. Xu, X. Chen, D. Li, X. Zhang, J. Zhu, Y. Ji and H. Song, *ACS Sustainable Chem. Eng.*, 2019, **7**, 8397–8404.
61 Y. Zhu, J. Zhu, H. Song, J. Huang, Z. Lu and G. Pan, *J. Rare Earths*, 2021, **39**, 374–379.
62 A. Wang, Y. Guo, Z. Zhou, X. Niu, Y. Wang, F. Muhammad, H. Li, T. Zhang, J. Wang, S. Nie and Z. Deng, *Chem. Sci.*, 2019, **10**, 4573–4579.
63 Z. Li, Z. Deng, A. Johnston, J. Luo, H. Chen, Y. Dong, R. Sabatini and E. H. Sargent, *Adv. Funct. Mater.*, 2022, **32**, 2111346.
64 C. Zhou, Y. Tian, M. Wang, A. Rose, T. Besara, N. K. Doyle, Z. Yuan, J. C. Wang, R. Clark, Y. Hu, T. Siegrist, S. Lin and B. Ma, *Angew. Chem., Int. Ed.*, 2017, **56**, 9018–9022.
65 H. Xiao, P. Dang, X. Yun, G. Li, Y. Wei, Y. Wei, X. Xiao, Y. Zhao, M. S. Molokeev, Z. Cheng and J. Lin, *Angew. Chem., Int. Ed.*, 2021, **60**, 3699–3707.
66 R. Lin, Q. Guo, Q. Zhu, Y. Zhu, W. Zheng and F. Huang, *Adv. Mater.*, 2019, **31**, e1905079.
67 B. Su, M. S. Molokeev and Z. Xia, *J. Phys. Chem. Lett.*, 2020, **11**, 2510–2517.
68 A. M. Anthony, M. K. Pandian, P. Pandurangan and M. Bhagavathiachari, *ACS Appl. Mater. Interfaces*, 2022, **14**, 29735–29743.
69 S. Zhao, C. Chen, W. Cai, R. Li, H. Li, S. Jiang, M. Liu and Z. Zang, *Adv. Opt. Mater.*, 2021, **9**, 2100307.
70 S. Fang, Y. Wang, H. Li, F. Fang, K. Jiang, Z. Liu, H. Li and Y. Shi, *J. Mater. Chem. C*, 2020, **8**, 4895–4901.
71 Q. Mo, J. Yu, C. Chen, W. Cai, S. Zhao, H. Li and Z. Zang, *Laser Photonics Rev.*, 2022, **16**, 2100600.
72 T. Jun, K. Sim, S. Iimura, M. Sasase, H. Kamioka, J. Kim and H. Hosono, *Adv. Mater.*, 2018, **30**, e1804547.
73 Z. Luo, Q. Li, L. Zhang, X. Wu, L. Tan, C. Zou, Y. Liu and Z. Quan, *Small*, 2020, **16**, e1905226.

74 H. Shao, X. Wu, J. Zhu, W. Xu, L. Xu, B. Dong, J. Hu, B. Dong, X. Bai, H. Cui and H. Song, *Chem. Eng. J.*, 2021, **413**, 127415.
75 S. Liu, X. Fang, B. Lu and D. Yan, *Nat. Commun.*, 2020, **11**, 4649.
76 X. Liu, Y. Yu, F. Yuan, C. Zhao, H. Dong, B. Jiao and Z. Wu, *ACS Appl. Mater. Interfaces*, 2020, **12**, 52967–52975.
77 S. Zhao, Q. Mo, W. Cai, H. Wang and Z. Zang, *Photonics Res.*, 2021, **9**, 187–192.
78 Q. Fan, G. V. Biesold-McGee, J. Ma, Q. Xu, S. Pan, J. Peng and Z. Lin, *Angew. Chem., Int. Ed.*, 2020, **59**, 1030–1046.
79 L. Wang, Z. Shi, Z. Ma, D. Yang, F. Zhang, X. Ji, M. Wang, X. Chen, G. Na, S. Chen, D. Wu, Y. Zhang, X. Li, L. Zhang and C. Shan, *Nano Lett.*, 2020, **20**, 3568–3576.
80 Z. Li, Z. Rao, Q. Li, L. Zhou, X. Zhao and X. Gong, *Adv. Opt. Mater.*, 2021, **9**, 2100804.
81 P. Zhu, S. Thapa, H. Zhu, S. Wheat, Y. Yue and D. Venugopal, *J. Alloys Compd.*, 2023, **960**, 170836.
82 B. Wang, X. Ouyang, X. He, Z. Deng, Y. Zhou and P. Li, *Adv. Opt. Mater.*, 2023, **11**, 2300388.
83 W. Ma, Q. Qian, S. M. H. Qaid, S. Zhao, D. Liang, W. Cai and Z. Zang, *Nano Lett.*, 2023, **23**, 8932–8939.
84 W. Ma, D. Liang, Q. Qian, Q. Mo, S. Zhao, W. Cai, J. Chen and Z. Zang, *eScience*, 2023, **3**, 100089.
85 Q. Chen, H. Fu, J. Jiang, Z. Fang, H. Zhang, W. Yang, W. Liu and J. Zheng, *J. Lumin.*, 2023, **258**, 119783.
86 M. Zhu, X. Du, G. Niu, W. Liu, W. Pan, J. Pang, W. Wang, C. Chen, Y. Xu and J. Tang, *Fundam. Res.*, 2022, **2**, 108–113.
87 D. Yan, S. Zhao, Y. Zhang, H. Wang and Z. Zang, *Opto-Electron. Adv.*, 2022, **5**, 200075.
88 Y. Zhou, J. Chen, O. M. Bakr and O. F. Mohammed, *ACS Energy Lett.*, 2021, **6**, 739–768.
89 B. Wang, D. Liang, S. M. H. Qaid, W. Cai, X. Yang, Z. Xu, R. Li, H. Xiao and Z. Zang, *Appl. Phys. Lett.*, 2024, **124**, 243302.
90 S. Bhaumik, S. Ray and S. K. Batabyal, *Mater. Today Chem.*, 2020, **18**, 100363.
91 A. Wang, X. Yan, M. Zhang, S. Sun, M. Yang, W. Shen, X. Pan, P. Wang and Z. Deng, *Chem. Mater.*, 2016, **28**, 8132–8140.
92 C. Sun, J.-P. Zang, Y.-Q. Liu, Q.-Q. Zhong, X.-X. Xing, J.-P. Li, C.-Y. Yue and X.-W. Lei, *CCS Chem.*, 2022, **4**, 3106–3121.
93 B. Wang, C. Wang, Y. Chu, H. Zhang, M. Sun, H. Wang, S. Wang and G. Zhao, *J. Alloys Compd.*, 2022, **910**, 164892.
94 M. Zhang, Z. Wang, B. Zhou, X. Jia, Q. Ma, N. Yuan, X. Zheng, J. Ding and W. H. Zhang, *Sol. RRL*, 2018, **2**, 1700213.
95 S. A. Kulkarni, S. G. Mhaisalkar, N. Mathews and P. P. Boix, *Small Methods*, 2019, **3**, 1800231.
96 H. Li, L. Tian, Z. Shi, Y. Li, C. Li, J. Feng and H. Zhang, *J. Mater. Chem. C*, 2022, **10**, 10609–10615.
97 A. Yangui, R. Roccanova, T. M. McWhorter, Y. Wu, M.-H. Du and B. Saparov, *Chem. Mater.*, 2019, **31**, 2983–2991.
98 J. Jiang, G. Niu, L. Sui, X. Wang, Y. Zhang, L. Che, G. Wu, K. Yuan and X. Yang, *J. Phys. Chem. Lett.*, 2021, **12**, 7285–7292.
99 S. Si, X. Guo, W. Gan, X. Zhang, B. Lan, M. R. Li and J. Wang, *J. Lumin.*, 2022, **251**, 119212.
100 Z. Tan, M. Hu, G. Niu, Q. Hu, J. Li, M. Leng, L. Gao and J. Tang, *Sci. Bull.*, 2019, **64**, 904–909.
101 J. Lu, C. Yan, W. Feng, X. Guan, K. Lin and Z. Wei, *EcoMat*, 2021, **3**, e12082.
102 X. Meng, S. Ji, Q. Wang, X. Wang, T. Bai, R. Zhang, B. Yang, Y. Li, Z. Shao, J. Jiang, K. L. Han and F. Liu, *Adv. Sci.*, 2022, **9**, e2203596.
103 S. Liu, Y. Yue, X. Zhang, C. Wang, G. Yang and D. Zhu, *J. Mater. Chem. C*, 2020, **8**, 8374–8379.
104 Z. Ma, Z. Shi, D. Yang, Y. Li, F. Zhang, L. Wang, X. Chen, D. Wu, Y. Tian, Y. Zhang, L. Zhang, X. Li and C. Shan, *Adv. Mater.*, 2021, **33**, e2001367.
105 B. Chiou, H. Lee, Y. Jang, Z. Yang, Y. Wang, M. Sarma, H. Su and K. Wong, *Org. Electron.*, 2017, **48**, 248–253.
106 S. Ye, F. Xiao, Y. X. Pan, Y. Y. Ma and Q. Y. Zhang, *Mater. Sci. Eng., R*, 2010, **71**, 1–34.
107 N. Narendran, J. D. Bullough, N. Maliyagoda and A. Bierman, *J. Illum. Eng. Soc.*, 2001, **30**, 57–67.
108 N. Narendran and Y. Gu, *J. Disp. Technol.*, 2005, **1**, 167–171.
109 G. Nedelcu, L. Protesescu, S. Yakunin, M. I. Bodnarchuk, M. J. Grotevent and M. V. Kovalenko, *Nano Lett.*, 2015, **15**, 5635–5640.
110 H. Chen, L. Zhu, C. Xue, P. Liu, X. Du, K. Wen, H. Zhang, L. Xu, C. Xiang, C. Lin, M. Qin, J. Zhang, T. Jiang, C. Yi, L. Cheng, C. Zhang, P. Yang, M. Niu, W. Xu, J. Lai, Y. Cao, J. Chang, H. Tian, Y. Jin, X. Lu, L. Jiang, N. Wang, W. Huang and J. Wang, *Nat. Commun.*, 2021, **12**, 1421.
111 Y. Zhang, Z. Zhang, W. Yu, Y. He, Z. Chen, L. Xiao, J. J. Shi, X. Guo, S. Wang and B. Qu, *Adv. Sci.*, 2022, **9**, e2102895.
112 D. Liu, X. Liu, Y. Gan, Z. Liu, G. Sun, C. Shen, X. Peng, W. Qiu, D. Li, Z. Zhou, Z. Li, H. L. Yip and S. J. Su, *ACS Energy Lett.*, 2022, **7**, 523–532.
113 T. Jun, T. Handa, K. Sim, S. Iimura, M. Sasase, J. Kim, Y. Kanemitsu and H. Hosono, *APL Mater.*, 2019, **7**, 111113.
114 Z. Ma, Z. Shi, C. Qin, M. Cui, D. Yang, X. Wang, L. Wang, X. Ji, X. Chen, J. Sun, D. Wu, Y. Zhang, X. J. Li, L. Zhang and C. Shan, *ACS Nano*, 2020, **14**, 4475–4486.
115 H. C. Jung-Min Heo, S.-C. Lee, M.-H. Park, J. S. Kim, H. Kim, J. Park, Y.-H. Kim, H. J. Yun, E. Yoon, D.-H. Kim, S. Ahn, S.-J. Kwon, C.-Y. Park and T.-W. Lee, *ACS Energy Lett.*, 2022, **7**, 2807–2815.
116 C. Zhou, H. Lin, Y. Tian, Z. Yuan, R. Clark, B. Chen, L. J. van de Burgt, J. C. Wang, Y. Zhou, K. Hanson, Q. J. Meisner, J. Neu, T. Besara, T. Siegrist, E. Lambers, P. Djurovich and B. Ma, *Chem. Sci.*, 2018, **9**, 586–593.
117 W. Liang, L. Wang, Y. Li, F. Zhang, X. Chen, D. Wu, Y. Tian, X. Li, C. Shan and Z. Shi, *Mater. Today Phys.*, 2021, **18**, 100398.
118 J. Chen, J. Wang, X. Xu, J. Li, J. Song, S. Lan, S. Liu, B. Cai, B. Han, J. T. Precht, D. Ginger and H. Zeng, *Nat. Photonics*, 2021, **15**, 238–244.
119 C. Y. Chang, A. N. Solodukhin, S. Y. Liao, K. P. O. Mahesh, C. L. Hsu, S. A. Ponomarenko, Y. N. Luponosov and Y. h. Chao, *J. Mater. Chem. C*, 2019, **7**, 8634–8642.

120 D. Y. Li, Y. H. Liu, Q. Wang, X. W. Lei, C. Y. Yue and Z. H. Jing, *Mater. Today Chem.*, 2023, **31**, e101604.
121 G. Xiong, L. Yuan, Y. Jin, H. Wu, Z. Li, B. Qu, G. Ju, L. Chen, S. Yang and Y. Hu, *Adv. Opt. Mater.*, 2020, **8**, e2000779.
122 J. Hou, J. Wu, Z. Qin, Y. Fang, L. Shen, X. Qiao, L. Dong, G. Zhang, Y. Liu, G. Zhao and H. Chen, *J. Mater. Chem. C*, 2023, **11**, 2137–2143.
123 J. Li, Y. Sheng, G. Tong, H. Zhu, X. Tao, C. Wu, Y. Chang, Z. Tang, J. Yang, S. Zhang and Y. Jiang, *Adv. Opt. Mater.*, 2023, **11**, e2300100.
124 Z. Li, G. Song, Y. Li, L. Wang, T. Zhou, Z. Lin and R. J. Xie, *J. Phys. Chem. Lett.*, 2020, **11**, 10164–10172.
125 H. Wang, C. Wang, Y. Wang, M. Sun and G. Zhao, *J. Phys. Chem. C*, 2023, **127**, 11616–11622.
126 Z. Li, Y. Li, P. Liang, T. Zhou, L. Wang and R. J. Xie, *Chem. Mater.*, 2019, **31**, 9363–9371.
127 Y. Sheng, P. Chen, Y. Gao, Y. He, J. Li, Muhammad, X. Xie, C. Cheng, J. Yang, Y. Chang, G. Tong and Y. Jiang, *ACS Appl. Mater. Interfaces*, 2024, **16**, 19175–19183.
128 Muhammad, Z. Liu, J. Li, Y. Sheng, Y. Chang, P. Chen and Y. Jiang, *J. Mater. Chem. C*, 2024, **12**, 6606–6614.
129 S. Li, Y. Zhao, L. Du, Y. He, R. Wang, Y. Guo, C. Wang, T. Tian, L. Wang and H. Liu, *Chem. Eng. J.*, 2024, **482**, 148966.
130 H. Xu, J. Liu, Q. Hu, J. Yu, Q. Han and W. Wu, *Adv. Opt. Mater.*, 2024, **12**, 2302288.
131 Z. Hu, X. Wang, K. Nie, R. Zhou, W. Dai, X. Duan, X. Zhang, H. Wang, L. Wang, L. Mei, Y. Liu and X. Ma, *Chem. Eng. J.*, 2024, **482**, 148829.
132 H. Mai, X. Wen, X. Li, N. S. L. Dissanayake, X. Sun, Y. Lu, T. C. Le, S. P. Russo, D. Chen, D. A. Winkler and R. A. Caruso, *Mater. Today*, 2024, **74**, 12–21.
133 D. Liang, X. Liu, B. Luo, Q. Qian, W. Cai, S. Zhao, J. Chen and Z. Zang, *EcoMat*, 2023, **5**, e12296.
134 A. K. Guria, S. K. Dutta, S. D. Adhikari and N. Pradhan, *ACS Energy Lett.*, 2017, **2**, 1014–1021.
135 X. Liu, X. Xu, B. Li, L. Yang, Q. Li, H. Jiang and D. Xu, *Small*, 2020, **16**, e2002547.
136 X. Deng, S. Cheng, X. Chen, M. Wang, X. Li, G. Li, D. Zhu, M. Jia, X. Li and Z. Shi, *J. Lumin.*, 2024, **269**, 120525.
137 F. Chen, X. Wang, X. Zhang and C. Zhang, *Opt. Mater.*, 2023, **139**, 113750.
138 G. Xu, C. Wang, Y. Li, W. Meng, G. Luo, M. Peng, B. Xu and Z. Deng, *Chem. Sci.*, 2023, **14**, 5309–5315.
139 W. Meng, C. Wang, Y. Li, G. Hu, S. Sui, G. Xu, M. Peng and Z. Deng, *Chem. - Eur. J.*, 2023, **29**, e202202675.
140 W. Zheng, R. Sun, Y. Liu, X. Wang, N. Liu, Y. Ji, L. Wang, H. Liu and Y. Zhang, *ACS Appl. Mater. Interfaces*, 2021, **13**, 6404–6410.
141 H. Xu, J. Yu, Q. Hu, Q. Han and W. Wu, *Mater. Today Chem.*, 2023, **30**, 101580.